J. Mech. Phys. Solids 191 (2024) 105762

Contents lists available at ScienceDirect

Journal of the Mechanics and Physics of Solids

journal homepage: www.elsevier.com/locate/jmps

Rainbow trapping of out-of-plane mechanical waves in spatially variant beam lattices

Bastian Telgen, Vignesh Kannan, Jean-Charles Bail, Charles Dorn, Hannah Niese, Dennis M. Kochmann *

Mechanics & Materials Lab, Department of Mechanical and Process Engineering, ETH Zürich, 8092 Zürich, Switzerland

ARTICLE INFO

Keywords:
Wave dispersion
Elasticity
Metamaterial
Truss

ABSTRACT

We numerically and experimentally investigate the propagation of mechanical waves in two-dimensional periodic and spatially graded elastic beam lattices. Experiments on metallic lattices admit the characterization of the linear elastic wave dispersion over a wide range of frequencies, resulting in complete, experimentally-constructed dispersion surfaces in excellent agreement with predictions obtained from finite element-based Bloch wave analysis. While Timoshenko beam theory is shown to be sufficiently accurate for predicting the lowest modes, experiments prove that solid finite elements are required to capture the dispersion relations at higher frequencies as well as when mode coupling occurs. Based on an improved numerical procedure, group velocity maps further highlight the directionality of wave dispersion and allow for the simple identification of bandgaps. In addition to classically studied periodic trusses, we extend the framework to spatially graded structures and demonstrate acoustic rainbow trapping in beam lattices undergoing out-of-plane vibrations. Our experiments confirm broadband vibration attenuation of the typical meta-wedge type previously observed only in optics and few mechanical studies. Results further show convincing agreement between Bloch theory-based predictions, finite element simulations, and experimental measurements. Such spatially-variant architected lattices show great promise for steering the motion of elastic waves in applications from wave guiding and wave shielding to energy harvesting.

1. Introduction

Although the propagation of elastic waves in heterogeneous periodic media is a rather old topic (Brillouin, 1946; Mead, 1973), it took until (Kushwaha et al., 1993) and Sigalas and Economou (1993) brought attention to the analogy to photonics (Joannopoulos et al., 1995) that the same principles were harnessed systematically for phononic and elastic wave motion, and for the creation of metamaterials for wave guidance. Inspired by the proposal of Yablonovitch (1987) for electromagnetic waves, early studies focused on realizing phononic bandgaps, i. e., frequency bands in which no elastic wave can travel, in two-phase composites (Vasseur et al., 1998; Liu, 2000; Sigmund and Jensen, 2003). As the interest in designing large bandgaps grew, several example realizations were reported for composites (Sigmund, 1994; Bilal and Hussein, 2011; D'Alessandro et al., 2016). Similarly, the early study of Langley et al. (1997) provided the blueprint for truss and beam lattices that admit wave guidance. The systematic exploration of bandgap engineering for wave attenuation and wave guidance started with, among others, the works of Ruzzene et al. (2003) and Phani et al. (2006).

* Corresponding author.
E-mail address: dmk@ethz.ch (D.M. Kochmann).
URL: https://mm.ethz.ch (D.M. Kochmann).

https://doi.org/10.1016/j.jmps.2024.105762
Received 30 December 2023; Received in revised form 29 May 2024; Accepted 30 June 2024
Available online 3 July 2024
0022-5096/© 2024 The Author(s). Published by Elsevier Ltd. This is an open access article under the CC BY license (http://creativecommons.org/licenses/by/4.0/).

As strut-based cellular architectures possess structurally appealing properties such as high specific stiffness and strength (Meza et al., 2017), a substantial scientific effort has gone into designing structural (meta-)materials with target properties. A popular and easily manufacturable example are truss lattices[1], and a key performance metric has been the as-designed steering or attenuation of waves. Wave guidance mainly leverages two physical principles. On the one hand, local resonance of structural members can lead to wide bandgaps (e.g., Gonella et al., 2009; Krödel et al., 2014; Matlack et al., 2016; Li et al., 2017; Bilal et al., 2021; Aguzzi et al., 2022). On the other hand, wave scattering in a periodic truss can attenuate waves, which has been exploited – along with local resonance – to achieve wave beaming, i.e., the guided motion of waves with strong directionality (see e.g., Ruzzene et al., 2003; Zelhofer and Kochmann, 2017; Casadei and Rimoli, 2013; Pal et al., 2016).

Key to understanding and predicting elastic wave motion in periodic media – such as periodic trusses – is the exploitation of Bloch's theorem (Bloch, 1929), which solves the equations of motion under the assumption of a traveling plane wave of arbitrary wavelength. The most popular techniques to numerically solve the associated Bloch eigenvalue problem include the Plane Wave Expansion Method (Sigalas and Economou, 1993; Kushwaha et al., 1993), the Multiple Scattering Method (Sigalas et al., 2009), and the Finite Element Method (Phani et al., 2006; Mace and Manconi, 2008; Hussein, 2009; Collet et al., 2011). For our purposes, we restrict ourselves to the Finite Element (FE) method for its maturity, accuracy, and generality. In an FE setting, Bloch's theorem can be enforced using Bloch boundary conditions applied to a periodic unit cell, or by substituting a Bloch operator into the governing equations. The two approaches are commonly referred to as the Bloch Boundary Condition Formulation (Mace and Manconi, 2008; Hussein, 2009) and the Bloch Operator Formulation (Collet et al., 2011), respectively. The former has the advantage of being compatible with a generic FE discretization but lacks the ability to obtain attenuation information, while the latter can resolve the complex-valued dispersion relation but requires FE discretization-specific derivations (Palermo and Marzani, 2020). To reduce the computational cost for band structure calculations (which can be significant when performing many repeated eigenvalue calculations to obtain dispersion surfaces), a number of order reductions schemes have been proposed (Krattiger and Hussein, 2017; Palermo and Marzani, 2020).

When it comes to wave motion in truss lattices, research so far has mainly focused on periodic structures, while the potential of leveraging spatially variant architectures, as demonstrated in photonics (Tsakmakidis et al., 2007; Rumpf et al., 2015), is yet to be fully realized. Only recently, Xie et al. (2018) and Zhao et al. (2020) suggested truss-based acoustic Luneburg lenses, using a density grading in a cubic truss lattice, which however does not extend to a rigorous mechanics treatment. Aguzzi et al. (2022) modified an octet truss by changing the mass of local resonators, which proved to be effective for generating broad bandgaps and guiding waves but offers a limited design space. Trainiti et al. (2017) reported wave filtering in graded lattices, but focused on only in-plane waves and used undulations to grade the lattice. The concepts of transformation elastodynamics have been applied to rich design spaces and resulted in successful examples of using spatially variant elastic properties to guide waves (Chen and Chan, 2010; Sun et al., 2019; Chang and Hu, 2012; Chen et al., 2016; Nassar et al., 2020); yet, this approach is limited to wave motion in the long-wavelength limit (without accounting for wave dispersion at higher frequencies, which gains importance in truss lattices). Very recently, the application of ray tracing techniques to mechanical waves has offered new opportunities for controlling wave motion through the design of spatially graded structures at high frequencies (Dorn and Kochmann, 2022, 2023b,a). Despite promising theoretical and numerical evidence of wave guidance and experimental proof of controlled wave transmissibility, their designs still lack experimental full-field confirmation of an effective wave control. In fact, almost all prior studies that experimentally probed wave motion in truss-based metamaterials assessed the success by measuring the transmissibility of waves through the medium – but lacked full-field measurements of the propagating waves.

In summary, although a few studies have previously used full-field experimental characterization of mechanical vibrations in cellular structures (Zhou et al., 2016; Trainiti et al., 2017; Schaeffer et al., 2017), their application to periodic and spatially graded truss lattices has been lacking, in particular, those undergoing out-of-plane deformation. Therefore, the aim of this study is two-fold. On the one hand, we demonstrate how full-field measurements of wave motion in periodic truss lattices can be used to experimentally characterize complete dispersion surfaces, which are shown to be in excellent agreement with predictions from FE-based Bloch wave analysis and furthermore shed light onto the accuracy of beam vs. solid FE representations. We select the orthorhombic lattice family with a rectangular base unit cell as a demonstrator and experimentally characterize waves in the lattice for different unit cell aspect ratios and across a wide range of frequencies (covering the lowest few dispersion surfaces). We also discuss the wave propagation characteristics in the different lattices by the help of an improved version of the directional group velocity maps of Zelhofer and Kochmann (2017). On the other hand, we exploit the knowledge gained from periodic lattices to understand and design wave attenuation in a spatially graded truss lattice. By combining different realizations of the orthorhombic unit cell into a graded lattice, we create an ultrawide phononic bandgap that realizes 'ultrasonic rainbow trapping' in a spatially variant architected lattice; i.e., we show experimentally (for the first time, to the best of our knowledge) that the combination of different unit cells in a graded lattice undergoing out-of-plane deformation can effectively superimpose individual bandgaps to achieve broadband wave attenuation. This extends previously demonstrated rainbow trapping in photonic metamaterials, (Tsakmakidis et al., 2007) as well as elastic pillar arrays (Colombi et al., 2016) and one-dimensional locally resonant mechanical metamaterials (De Ponti et al., 2020), to the new setting of two-dimensional truss lattices.

The remainder of this contribution is organized as follows. Section 2 reviews the relevant theory of elastodynamics in periodic media and the resulting dispersion relations and directional group velocity. In Section 3, we introduce the experimental setup

[1] Here and in the following, we use the term *truss lattice* to refer to periodic assemblies of struts that may undergo stretching and bending (and torsion in three dimensions). Though the FE community may differentiate between trusses (composed of pin-jointed bars) and frames (assuming welded beams), we here use the term *truss* for all such structural assemblies, as is common in the metamaterials literature.

to validate the presented methods and observe wave motion in trusses. Section 4 describes the numerical treatment of Bloch wave analysis and time-transient simulations. Section 5 summarizes the results, including the experimental characterization of the dispersion relations of periodic square (Section 5.1) and rectangular lattices (Section 5.2) as well as results for the spatially variant lattice (Section 5.3). Finally, Section 6 concludes this study.

2. Elastodynamics of periodic media

Let us briefly review the theory of wave dispersion in periodic elastic media as a foundation for the subsequent discussions. For a more detailed treatment of the topic, the reader is referred to, e.g., Hussein et al. (2014) and Phani and Hussein (2017).

The propagation of small-amplitude stress waves in a linear elastic body $\Omega \subset \mathbb{R}^d$ in d dimensions is governed by the balance of linear momentum, which – neglecting the influence of body forces – is written as

$$\operatorname{div} \boldsymbol{\sigma} = \rho \ddot{\boldsymbol{u}}, \tag{1}$$

where $\boldsymbol{u} : \Omega \times \mathbb{R} \to \mathbb{R}^d$ is the displacement field depending on position $\boldsymbol{x} \in \Omega$ and time t, ρ is the mass density, and $\boldsymbol{\sigma}$ the infinitesimal (Cauchy) stress tensor with components $\sigma_{ij} = \mathbb{C}_{ijkl}\varepsilon_{kl}$ in a Euclidean basis, where $\varepsilon_{ij} = \frac{1}{2}(u_{i,j} + u_{j,i})$ denotes the infinitesimal strain tensor, and minor symmetry of $\mathbb{C}$ further reduces the above to $\sigma_{ij} = \mathbb{C}_{ijkl}u_{k,l}$. Here and in the following, we imply Einstein's summation convention over repeated indices, and we abbreviate partial spatial derivatives by indices following a comma. $\mathbb{C}$ is the fourth-order elasticity tensor, whose components $\mathbb{C}_{ijkl}$ satisfy major and minor symmetry. Owing to the separable form of Eq. (1) in the linear elastic case, linear waves assume the form of a time-harmonic displacement field

$$\boldsymbol{u}(\boldsymbol{x}, t) = \hat{\boldsymbol{u}}(\boldsymbol{x}, \omega) e^{-i\omega t}, \tag{2}$$

whose amplitude field $\hat{\boldsymbol{u}} : \Omega \to \mathbb{C}^d$ is generally complex-valued, while the frequency $\omega \in \mathbb{R}$ is real-valued in a linear elastic medium. Inserting (2) into (1) with $\sigma_{ij} = \mathbb{C}_{ijkl}u_{k,l}$ yields the differential equation

$$\mathbb{C}_{ijkl}\hat{u}_{k,jl} + \mathbb{C}_{ijkl,j}\hat{u}_{k,l} + \rho\omega^2\hat{u}_i = 0, \tag{3}$$

which can in general be solved for pairs of frequency ω and associated amplitude field $\hat{\boldsymbol{u}}$.

When applying the above relations to waves in metamaterials, we exploit that a periodic medium is characterized as a simple Bravais lattice (Bravais, 1850) by invariance under any discrete lattice translation

$$\boldsymbol{R} = \sum_{i=1}^{d} n_i \boldsymbol{a}_i \qquad \text{with} \quad n_i \in \mathbb{Z}, \tag{4}$$

where $\{\boldsymbol{a}_1, \dots, \boldsymbol{a}_d\}$ denote the linearly independent lattice basis vectors. For a periodic linear elastic solid, the periodicity in (4) translates into a periodic mass density and elasticity tensor, i.e., respectively,

$$\rho(\boldsymbol{x} + \boldsymbol{R}) = \rho(\boldsymbol{x}), \qquad \mathbb{C}(\boldsymbol{x} + \boldsymbol{R}) = \mathbb{C}(\boldsymbol{x}). \tag{5}$$

Periodicity further admits the identification of a unit cell Ω_{UC}, such that every position $\boldsymbol{x} \in \Omega$ in the infinite, periodic medium is uniquely linked to a position $\boldsymbol{x}_{\mathrm{UC}} \in \Omega_{\mathrm{UC}}$ inside the unit cell by $\boldsymbol{x} = \boldsymbol{x}_{\mathrm{UC}} + \boldsymbol{R}$ with a unique set of integers $\{n_1, \dots, n_d\}$ in (4). The choice of the unit cell is, of course, not unique. In fact, the choice of both unit cell and lattice vectors is infinite. For convenience, we choose a primitive unit cell, i.e., the smallest possible unit cell spanned by a set of primitive lattice vectors $\{\boldsymbol{a}_1^{\mathrm{prim}}, \dots, \boldsymbol{a}_d^{\mathrm{prim}}\}$ such that $\|\Omega_{\mathrm{UC}}\| = \|\det(\boldsymbol{a}_1^{\mathrm{prim}}, \dots, \boldsymbol{a}_d^{\mathrm{prim}})\|$, which we simply refer to as the *unit cell* (UC) in the following.

For a periodic medium as characterized by (4), Bloch's theorem states that for any pair $(\omega, \hat{\boldsymbol{u}})$ that satisfies (3), there exists at least one wave vector $\boldsymbol{k} \in \mathbb{C}^d$ such that the displacement field (2) under a discrete lattice translation $\boldsymbol{R}$ according to (4) is modulated by a plane wave with that wave vector (Bloch, 1929), i.e.,

$$\hat{\boldsymbol{u}}(\boldsymbol{x} + \boldsymbol{R}, \omega; \boldsymbol{k}) = \hat{\boldsymbol{u}}(\boldsymbol{x}, \omega; \boldsymbol{k})\, e^{i\boldsymbol{k}\cdot\boldsymbol{R}}, \tag{6}$$

where we denote by $\hat{\boldsymbol{u}}(\boldsymbol{x}, \omega; \boldsymbol{k})$ the mode shape $\hat{\boldsymbol{u}}(\boldsymbol{x}, \omega)$ for a given $\boldsymbol{k}$-vector. Exploiting Bloch's theorem (6) in conjunction with the periodicity of the medium, we realize that

$$\hat{\boldsymbol{u}}(\boldsymbol{x}, \omega; \boldsymbol{k}) = \hat{\boldsymbol{u}}(\boldsymbol{x}_{\mathrm{UC}} + \boldsymbol{R}, \omega; \boldsymbol{k}) = \hat{\boldsymbol{u}}(\boldsymbol{x}_{\mathrm{UC}}, \omega; \boldsymbol{k})\, e^{i\boldsymbol{k}\cdot\boldsymbol{R}}, \tag{7}$$

so that the governing equations of wave motion in a periodic elastic medium can be reduced to solving the following boundary value problem on the UC:

$$\begin{cases} \mathbb{C}_{ijkl}\hat{u}_{k,jl} + \mathbb{C}_{ijkl,j}\hat{u}_{k,l} + \rho\omega^2\hat{u}_i = 0 & \text{in } \Omega_{\mathrm{UC}}, \\ \hat{u}_i^{+} = \hat{u}_i^{-} e^{i\boldsymbol{k}\cdot\boldsymbol{R}} & \text{on } \partial\Omega_{\mathrm{UC}}, \end{cases} \tag{8}$$

where $\hat{\boldsymbol{u}}^{\pm} = \hat{\boldsymbol{u}}(\boldsymbol{x}_{\pm})$ are the displacements of pairs of periodically opposite points $\boldsymbol{x}_{\pm}$ on the unit cell's outer boundary $\partial\Omega_{\mathrm{UC}}$. Eq. (8) is also referred to as the Bloch boundary condition formulation (Mace and Manconi, 2008).

The propagation of waves in a periodic medium is effectively described by the *dispersion relation*, which links wave vector $\boldsymbol{k} \in \mathbb{C}^d$ to frequency $\omega \in \mathbb{R}$. A numerically convenient way to obtain that relation is to solve the generalized eigenvalue problem resulting from (8) with appropriate Bloch boundary conditions for all pairs $(\omega_n, \hat{\boldsymbol{u}}_n)$, and to repeat this procedure for all relevant $\boldsymbol{k}$-vectors.

This leads to dispersion relations of the type $\omega_j = \omega_j(\boldsymbol{k})$, the jth solution corresponding to the jth mode of the system. The generally complex-valued wave vector $\boldsymbol{k} = \boldsymbol{\mu} + i\boldsymbol{\delta}$ contains information about the attenuation (or growth) $\boldsymbol{\mu}$ and the phase $\boldsymbol{\delta}$ of a wave traveling through the periodic medium. For ease of simulations and since we here are primarily interested in wave motion outside of bandgaps, we here neglect the attenuation ($\boldsymbol{\mu} = \boldsymbol{0}$) and consider lossless wave motion in the elastic medium, so that $\boldsymbol{k} \in \mathbb{R}^d$.

The resulting wave vectors $\boldsymbol{k} \in \mathbb{R}^d$ live in a reciprocal space, which – analogous to the physical lattice satisfying (4) – is invariant under reciprocal lattice translations

$$\boldsymbol{G} = \sum_{i=1}^{d} m_i \boldsymbol{b}_i \qquad \text{with} \qquad m_i \in \mathbb{Z}, \tag{9}$$

where $\{m_1, \dots, m_d\}$ is a unique set of integers, and the reciprocal lattice vectors $\{\boldsymbol{b}_1, \dots, \boldsymbol{b}_d\}$ are related to the physical basis vectors $\{\boldsymbol{a}_1, \dots, \boldsymbol{a}_d\}$ by the relation $\boldsymbol{a}_i \cdot \boldsymbol{b}_j = 2\pi\delta_{ij}$, using Kronecker's delta. As a consequence, the complete dispersion information is contained within a primitive unit cell in reciprocal space (Brillouin, 1946), known as the *First Brillouin Zone* U_{FBZ} and spanned by the reciprocal lattice vectors $\{\boldsymbol{b}_1, \dots, \boldsymbol{b}_d\}$. Moreover, if the UC possess certain symmetries, a subdomain of U_{FBZ} can contain the full dispersion information of the unit cell. The smallest such domain that contains all dispersion information is the *Irreducible Brillouin Zone* U_{IBZ} (see Fig. 2). When computing the dispersion relations in practice, it is therefore sufficient to sample over $\boldsymbol{k}$-vectors only from within U_{IBZ}. Corners of the Irreducible Brillouin Zone are high symmetry points in reciprocal space, and often the edges connecting the high symmetry points are considered to be representative of the global dispersion behavior (Hussein et al., 2014).

We close by noting that the dispersion relation contains information about the *group velocity* $\boldsymbol{v}_g$, which indicates the direction and speed of a wave packet and hence the direction of energy flow during wave motion. For $\boldsymbol{k} \in \mathbb{R}^d$, it is obtained as

$$\boldsymbol{v}_g(\boldsymbol{k}) = \frac{\partial \omega(\boldsymbol{k})}{\partial \boldsymbol{k}}. \tag{10}$$

$v_g = |\boldsymbol{v}_g|$ serves as an excellent indicator for wave guiding, since it correlates well with other commonly used indicators such as, e.g., the maximum displacement or velocity amplitudes of propagating waves (Zelhofer and Kochmann, 2017). Frequency ranges that are not covered by any dispersion surface for all real wave vectors $\boldsymbol{k}$ (and for which hence no group velocity exists), are referred to as *complete bandgaps*. By contrast, *directional bandgaps* imply that wave packets travel only in certain directions. All other cases are referred to as *pass bands*.

3. Experiments

3.1. Sample design and manufacturing

Truss lattices with rectangular unit cells were laser-cut out of thin square plates made of aluminum alloy 6061-T6, having dimensions 40 × 40 cm and thickness $h = 1$ mm. An aluminum alloy was chosen for ease of manufacturing and to ensure a linear elastic material response with little wave attenuation. Prior studies have typically utilized 3D-printed polymer lattices and metamaterials to investigate wave motion, which, unfortunately, makes it non-trivial to decouple wave attenuation and dispersion due to material-intrinsic viscoelastic damping and lattice topology. Here, by contrast, the chosen metallic samples admit approximately linear elastic wave motion with minimal artifacts of damping. A lattice spacing of $L = 5$ mm along the x-direction and a beam width $w \approx 500$ μm were chosen. The resulting beam slenderness ratio is $h/L \leq 0.2$. Four different types of structured plates were manufactured with different unit cell aspect ratios: periodic lattices with aspect ratios $\gamma = 1$, $\gamma = 1.3$, and $\gamma = 2$, as well as a spatially graded lattice, whose aspect ratio varies in the vertical direction between $\gamma = 1$ at the center and $\gamma = 2$ at the top and bottom, as shown in Fig. 2.

3.2. Experimental setup

The experimental setup is shown in Fig. 1. A piezoelectric transducer (ThorLabs PA3CBW) was glued to the center of each truss plate with superglue. The transducer achieved a maximum displacement of 1 μm with maximum and resonant frequencies of 1 MHz and 920 kHz, respectively. The transducer was actuated by a high-voltage amplifier (ThorLabs HVA200) with input from an arbitrary function generator (Teledyne T3AFG40). The input signals were recorded using an external digital oscilloscope (Tektronix TBS2000 series) for real-time diagnostics.

Wave propagation was captured using a Scanning Laser Doppler Vibrometer (SLDV; Optomet SWIR) with an infrared laser source (wavelength 1550 nm). Out-of-plane particle velocities were measured as a function of space and time with a maximum measurable velocity set at 490 mm/s. Data was collected using a built-in data acquisition unit at 32-bit resolution. Due to the relatively low volume fraction of material in the structured plates, a custom grid was designed for laser scanning. The spatial resolution of scanning was set to ∼ 1 mm (5–10 points per unit cell edge) with sampling frequencies of at least 2 MHz (temporal resolution 500 ns). For the frequency analysis, spectral resolutions of 1 kHz and 250 Hz were explored. While the data quality with the latter was clearly better, both were adequate to capture dispersion in frequency–wavenumber space.

Triggering of the data acquisition system (integrated in the SLDV) was critical to measure the traveling wavefront, as opposed to conventional steady-state vibrations. The wavefronts were captured using separate transducer excitation events for every spatial point recorded. The input signal was generated by the function generator in bursts with a time period of 2 seconds. The burst period was chosen to wait for complete attenuation of wave reflections from sample edges. To synchronize measurements from each spatial

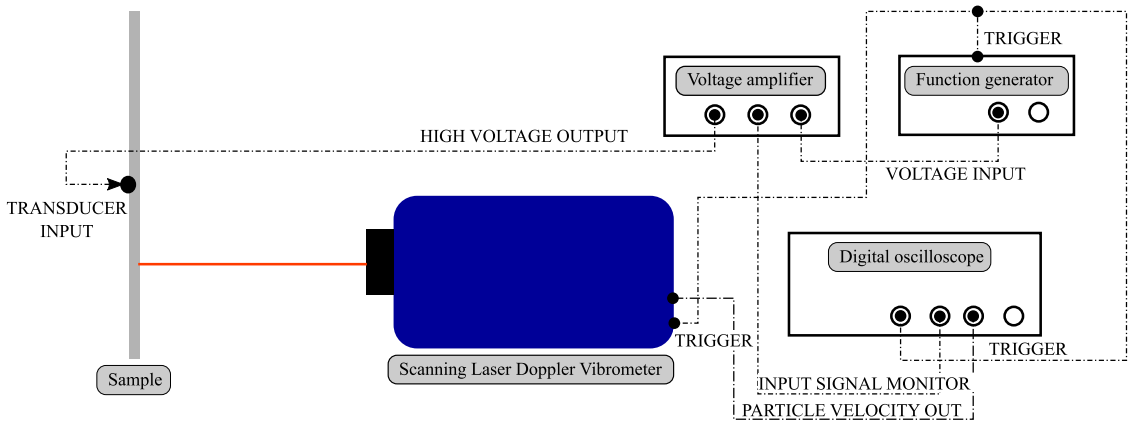

Fig. 1. Experimental setup: the aluminum truss plate is clamped vertically and excited by a piezo-transducer at its center, while a Scanning Laser Doppler Vibrometer is used to capture the out-of-plane velocity profile of the vibrating sample.

point, a 3 V transistor-to-transistor logic (TTL) trigger pulse was sent at the start of each burst from the function generator to the oscilloscope and the data acquisition system of the SLDV to record data. At least five samples were recorded and averaged at each spatial point for postprocessing.

Linear frequency chirp signals at three different center frequencies were used as input to the transducer to span a wide frequency spectrum. (Fig. 12 in Appendix A shows the velocity measured at the excitation point and its frequency spectrum for one of three different chirp signals used in experiments.) A low-pass filter with a cut-off frequency of 500 kHz was applied to all signals. The primary difference between the three signals is in the frequency content. While the spectral amplitudes of the input signal to the transducer were nominally constant, the transfer function of the transducer as a function of frequency (i.e., the ratio of output to input power, $\mathcal{P}^{(\text{out})}/\mathcal{P}^{(\text{in})}(\omega)$) is not. The data in Appendix A (see Fig. 12), however, shows that this effect is not significant, especially in the frequency range of interest. Snapshots at $t = 150\mu s$ for chirp signal 1 are also shown in Appendix A (Fig. 13) for different truss lattices.

3.3. Data analysis

The experimental data was analyzed with the aim of characterizing the real-time propagation of out-of-plane waves fronts in 2D lattices as well as their signal peaks in wavenumber-frequency (k_x-k_y-ω) space. Rather than obtaining the transmissibility at dedicated frequencies or along high-symmetry paths in the FBZ, which is common in the literature, our protocol extracts complete dispersion surfaces of the lowest few modes purely from experimental data as follows. The spatio-temporal out-of-plane particle velocities from the data acquisition system of the SLDV were re-cast into a matrix $v(x, y, t)$. A spatio-temporal tapered cosine window $\mathcal{T}(x, y, t) = \hat{\mathcal{T}}(x, y)\tilde{\mathcal{T}}(t)$ was used to smoothly remove data from the edges of the plate and at long times. The windowed velocity data was calculated as $\hat{v}(x, y, t) = \hat{\mathcal{T}}(x, y)\tilde{\mathcal{T}}(t)v(x, y, t)$. To reduce noise, a low-pass Butterworth filter of order 15 and cut-off frequency 500 kHz was used on the windowed velocity data. The filtered velocity data is denoted by $\bar{v}(x, y, t)$. To compute dispersion surfaces, a 3D Fast Fourier Transform (FFT) was performed on $\bar{v}(x, y, t)$, using the fftn function of the *numpy* package in Python. The 3D FFT data, $V(k_x, k_y, \omega)$, was normalized by the 'volume' of the Fourier space ($V = N_x N_y N_t$, where N_x, N_y, N_t are the numbers of sampled points in the x-direction, y-direction, and time, respectively) to present an analogue of the elastic energy density in Fourier space. The magnitude of the 3D FFT data was normalized by that of the temporal Fourier transform of the particle velocity $V_0(t)$ at the point of excitation, resulting in the normalized Fourier transform $V(k_x, k_y, \omega)/V_0(\omega)$. For data representation, we use both the normalized Fourier transform and the power spectral density, $\mathcal{P} = 20\log_{10}(\|V\|/\|V_0\|)$. In addition, 1D Fourier transforms were computed along the time axis for each spatial point (denoted as $\tilde{V}(x, y, \omega)$). This representation is used to illustrate the effects of spatial wave guiding in the spatially-graded samples.

4. Simulations

4.1. Wave finite element method

Based on the theory introduced in Section 2, we solve the governing Eqs. (8) by the Wave Finite Element Method (WFEM) (Mace and Manconi, 2008; Hussein, 2009), which relies on an FE discretization in space. All simulations have been performed in ae108 (Weberndorfer), a scalable variational framework for FE analysis. The harmonic eigenvalue problem (8) assumes the discretized form

$$\left(\boldsymbol{K} - \omega^2 \boldsymbol{M}\right)\hat{\boldsymbol{U}} = \boldsymbol{0} \tag{11}$$

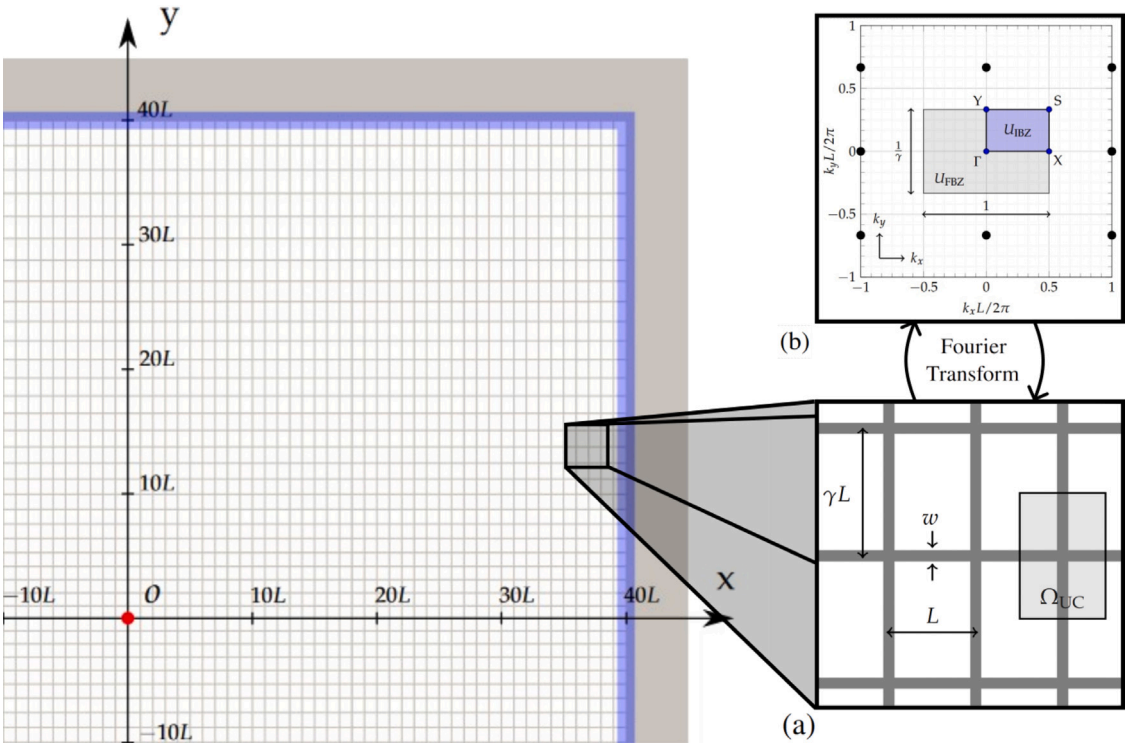

Fig. 2. First quadrant of a rectangular lattice that is linearly graded in the y-direction. At the origin, at $y = 0$, the lattice has an aspect ratio of $\gamma = 1$, whereas at the top and bottom borders, at $y = \pm 40L$, the aspect ratio is $\gamma = 2$. The excitation node O at the origin is marked by a red dot. In transient simulations, all nodes in the shaded blue areas are fixed. **(a)** Locally, the rectangular truss lattice is assumed to be (quasi-)periodic with characteristic beam length L and unit cell aspect ratio γ. The rectangular cross-sections of all struts have width $w = L/10$ and out-of-plane thickness $h = L/5$. The gray area depicts the chosen *representative unit cell* Ω_{UC} in real space. **(b)** In reciprocal space, the *First Brillouin Zone* U_{FBZ} and the *Irreducible Brillouin Zone* U_{IBZ} are depicted in gray and blue, respectively. The path along the circumference of the IBZ through high-symmetry points Γ, X, S, and Y is referred to as the high-symmetry path.

with the global stiffness matrix $\boldsymbol{K}$, global consistent mass matrix $\boldsymbol{M}$, and a global harmonic displacement vector $\boldsymbol{U}(t) = \hat{\boldsymbol{U}} e^{i\omega t}$ with amplitude vector $\hat{\boldsymbol{U}} \in \mathbb{C}^{n_d}$ for an FE mesh having n_d degrees of freedom.

Bloch boundary conditions $(8)_2$ link the nodal displacement amplitudes according to

$$\hat{\boldsymbol{u}}(\boldsymbol{x}^+) = e^{i\boldsymbol{k}\cdot(\boldsymbol{x}^+ - \boldsymbol{x}^-)} \hat{\boldsymbol{u}}(\boldsymbol{x}^-) \tag{12}$$

for all periodic pairs of nodes on opposite faces (or edges) of the unit cell. In the discrete setting, this admits defining a set of target nodes having displacements $\boldsymbol{U}^+$, and a set of source nodes with displacements $\boldsymbol{U}^-$: the latter are independent degrees of freedom of the unit cell, while the former are slave to the latter via a linear transformation

$$\hat{\boldsymbol{U}}^+ = \boldsymbol{P}(\boldsymbol{k}) \hat{\boldsymbol{U}}^-, \tag{13}$$

where $\boldsymbol{P}(\boldsymbol{k})$ is called the transformation matrix dependent on $\boldsymbol{k}$ through (12). From (11) and (13) follows the generalized eigenvalue problem

$$\left[\tilde{\boldsymbol{K}}(\boldsymbol{k}) - \omega^2 \tilde{\boldsymbol{M}}(\boldsymbol{k})\right] \hat{\boldsymbol{U}}^- = \boldsymbol{0} \qquad \text{with} \quad \tilde{\boldsymbol{K}}(\boldsymbol{k}) = \boldsymbol{P}^*(\boldsymbol{k}) \boldsymbol{K} \boldsymbol{P}(\boldsymbol{k}), \quad \tilde{\boldsymbol{M}}(\boldsymbol{k}) = \boldsymbol{P}^*(\boldsymbol{k}) \boldsymbol{M} \boldsymbol{P}(\boldsymbol{k}), \tag{14}$$

where $(\cdot)^*$ indicates the conjugate transpose of a matrix. Note that due to the definition of $\boldsymbol{P}$ in our problem, $\tilde{\boldsymbol{K}}$ and $\tilde{\boldsymbol{M}}$ are positive-(semi-)definite, which results in $\omega^2 \geq 0$ and real-valued eigenvectors $\hat{\boldsymbol{U}}^-$. To solve the eigenvalue problem (14) for pairs $(\omega_j, \hat{\boldsymbol{U}}_j^-)$ for a given $\boldsymbol{k}$-vector from the IBZ, we apply a Shift and Invert Spectral Transformation to the problem and use the Krylov-Schur algorithm to compute n_e eigenpairs with smallest eigenvalue magnitude corresponding to the n_e lowest modes of the system, using the Scalable Library for Eigenvalue Problem Computations (SLEPc) (Hernandez et al., 2005). In a final step, the eigenvector $\hat{\boldsymbol{U}}_j^-$ is transformed by (13) to obtain the complete displacement amplitude vector $\hat{\boldsymbol{U}}_j$ representing the physical mode shape.

We evaluate the eigenfrequencies $\omega_j(\boldsymbol{k})$ on an equally-spaced grid of 200 × 200 $\boldsymbol{k}$-vectors in the reciprocal IBZ, resulting in a discrete approximation of the dispersion surface for each mode j. When presenting results in subsequent sections, we generally report the normalized frequency

$$\bar{f} = \frac{fL}{c} = \frac{\omega L}{2\pi c}, \tag{15}$$

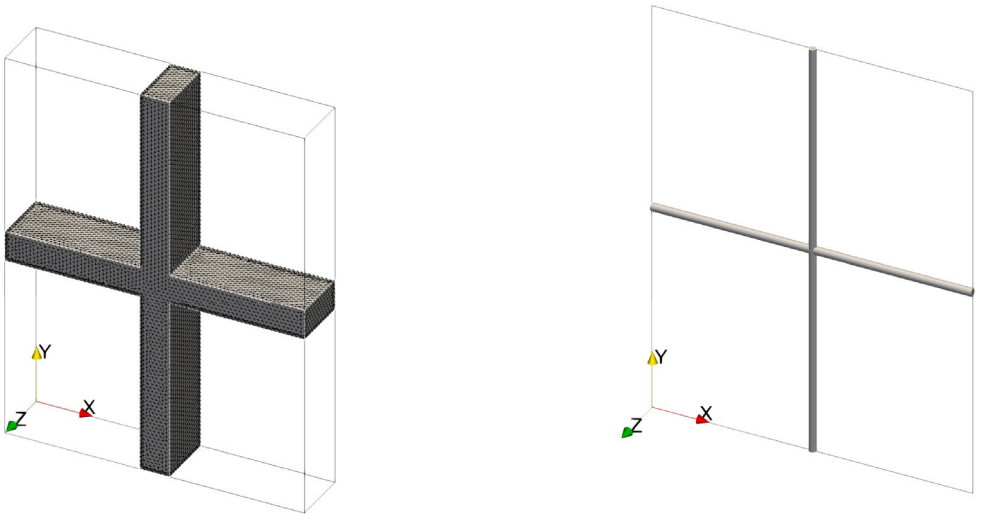

(a) (b)

Fig. 3. A *representative unit cell* Ω_{UC} of a rectangular truss lattice with aspect ratio $\gamma = 1.3$ discretized using (a) solid finite elements and (b) Timoshenko beam elements. The solid FE mesh uses linear tetrahedral elements with a maximum edge length of $w/8$. A periodic mesh is ensured by copying the boundary mesh from source to target boundaries. Alternatively, we use Timoshenko beam elements with a maximum element length of $L/20$ for computational efficiency.

where $c = \sqrt{E/\rho}$ is the longitudinal wave speed within a homogeneous strut of Young's modulus E and mass density ρ. By symmetry, we consider only the Irreducible Brillouin Zone U_{IBZ} and extend the data onto U_{FBZ} for computational efficiency. Besides full dispersion surfaces, we compute the dispersion relation along the high-symmetry path Γ-X-S-Y-Γ (see Fig. 2(b)).

In subsequent examples, we study wave propagation in 2D truss lattices, which in general undergo longitudinal and flexural motion both within and out of the plane spanned by the truss lattice. To identify out-of-plane modes (which are the ones tracked in experiments later), we introduce the *out-of-plane ratio* of a mode j as

$$\beta_j = \frac{\left|\hat{\boldsymbol{U}}_j^z\right|}{\left|\hat{\boldsymbol{U}}_j\right|} \in [0,1], \tag{16}$$

where $\hat{\boldsymbol{U}}_j^z$ is the (real part of the) amplitude vector of mode j, containing only displacements in the out-of-plane z-direction. Rotational degrees of freedom, as part of beam theory, are not considered here. $\beta_j \approx 1$ is an out-of-plane mode, whereas $\beta_j \approx 0$ implies an in-plane mode. To capture all primarily out-of-plane modes, we include in our investigation all modes with $\beta_j > 0.1$. (In practice, we observe that mixed modes occur mainly at higher frequencies and have little relevance in this study.)

To better understand the directionality of wave motion, we extract from the dispersion relations the group velocity $\boldsymbol{v}_g$ of wave packets traveling at a given frequency, by modifying the approach of Zelhofer and Kochmann (2017). To differentiate $\omega_j(\boldsymbol{k})$ with respect to $\boldsymbol{k}$ (as required in (10)), we interpolate the dispersion surfaces $\omega_j(\boldsymbol{k})$ using bivariate cubic splines over a rectangular grid to guarantee (at least) C^1-continuity, which admits the computation of the group velocity in (10) from the splines by differentiation. When discussing results, we will report the *normalized group velocity*

$$\bar{v}_g = |\boldsymbol{v}_g|/c. \tag{17}$$

The group velocity $\boldsymbol{v}_g^j(\boldsymbol{k})$ is evaluated for each dispersion surface j over the entire FBZ on an evenly spaced grid of 2000 × 2000 $\boldsymbol{k}$-points in reciprocal space, resulting in $4 \cdot 10^6$ data points. At each $\boldsymbol{k}$-point, we compute $\boldsymbol{v}_g^j(\boldsymbol{k})$ and decompose it into its speed $v_g^j = |\boldsymbol{v}_g^j(\boldsymbol{k})|$ and direction $\theta_j(\boldsymbol{k})$ in the 2D plane of the lattice. We generate a group velocity map by plotting each pair $\left(v_g^j(\boldsymbol{k}), \theta_j(\boldsymbol{k})\right)$ (for each $\boldsymbol{k}$-point and for each of the lowest few dispersion surfaces j) as a point in a polar plot, as shown in Fig. 7. Radial rays imply a constant direction θ, while circles of fixed radius contain iso-frequency information. The color code indicates the group velocity v_g^j. Wherever the data from two (or more) modes overlap, we present the mode with the highest group velocity, as that mode is expected to be observed first in transient wave motion. (However, we generally note that, for some directions and frequencies, different modes might support different wave packet speeds.) Points in the polar plot that remain white do not support any group velocity and hence indicate bandgaps. Note that, in contrast to Zelhofer and Kochmann (2017), we include in the group velocity maps every interpolated data point of the 2000 × 2000 grid, which avoids the distortions around the band gaps seen in Zelhofer and Kochmann (2017).

Table 1
Material properties of aluminum alloy 6061-T6 used in simulations.

E [GPa]	ν [–]	ρ [kg/m^3]
69	1/3	2700

4.2. Transient wave analysis

For a comparison with results from Bloch wave analysis, we also perform dynamic FE simulations of entire trusses. A time-harmonic out-of-plane excitation is applied at the truss' center (see Fig. 2), for which the propagating waves are simulated over time by integrating the FE equations of motion using an implicit Newmark-β scheme (with $\beta = 1/4$ and $\gamma = 1/2$ to avoid numerical damping). We impose the excitation by prescribing the out-of-plane displacement, velocity, and acceleration of the center node at each time step according to, respectively,

$$u_o^z(t) = \hat{u}_o \sin(\omega t), \qquad \dot{u}_o^z(t) = \omega \hat{u}_o \cos(\omega t), \qquad \ddot{u}_o^z(t) = -\omega^2 \hat{u}_o \sin(\omega t), \tag{18}$$

with an arbitrary amplitude $\hat{u}_o \in \mathbb{R}$ and a prescribed frequency $\omega > 0$. Nodes on the outer boundary (i. e., all nodes in the blue shaded region in Fig. 2) are fixed with clamped boundary conditions. We stop all simulations before any wave reaches the blue region to prevent wave reflection and the resulting interference.

4.3. Finite element discretization

Both Bloch wave analysis (Section 4.1) and transient wave analysis (Section 4.2) require a choice of the FE discretization. In subsequent simulations, we use – separately – two types of FE representations: (i) fully resolved solid elements, specifically three-dimensional (3D) constant-strain tetrahedral (CST) elements, and (ii) 2-node Timoshenko beam elements. For a CST mesh, a maximum element edge length of $w/8$ (see Fig. 3) is enforced for reasons of accuracy, and an isotropic linear elastic material is assumed with Young modulus E and Poisson ratio $\nu = 1/3$. The (consistent) mass matrix $\boldsymbol{M}$ is based on a homogeneous mass density ρ. While this solid discretization is highly accurate and especially used for Bloch wave analysis in the following, it becomes prohibitively expensive for discrete numerical calculations on large trusses. Therefore, we also use a Timoshenko beam representation, using 20 beam elements per length L (see Fig. 3). Beam elements use the same linear elastic constitutive law (Young's modulus E) and mass density ρ, and a shear coefficient (Cowper, 1966) of

$$\kappa_o = \frac{10(1+\nu)}{12+11\nu} \tag{19}$$

with Poisson's ratio $\nu = 1/3$. The choice of the shear coefficient is not unique (Kaneko, 1975). While (19) is generally accepted as applicable to most static applications, among others Hutchinson (1981) reported that it depends on the wave frequency ω when used in a dynamic setting, so the static shear coefficient κ_o is only applicable at low frequencies. Le (1999) introduced shear coefficients for dynamic analysis. However, as those require careful tuning and our focus is on the lowest eigenmodes only, we accept possible inaccuracies at high frequencies (which will become apparent from comparison to the fully resolved solid element discretization). Note also that beam elements cannot properly capture the mechanics of beam junctions (Portela et al., 2018) – an effect that increases with decreasing beam slenderness L/h. As we here deal with beams of moderate slenderness $L/h \geq 5$, the effect is expected to be small. For simulations with both types of FE discretizations, we use the material properties in Table 1 for aluminum alloy 6061-T6, which is used in our experiments. (Note that all reported normalized data do not depend on the specific values of E and ρ.)

5. Results

In the following, we first investigate wave dispersion in two periodic lattices with different unit cell aspect ratios (comparing experimental data to simulation results and thus validating the results from Bloch wave analysis as well as demonstrating the experimental extraction of dispersion surfaces), before examining the case of a spatially graded lattice.

5.1. Square lattice

For the square lattice with an aspect ratio of $\gamma = 1$, the calculated (normalized) dispersion relation $\bar{f}(\boldsymbol{k})$ within the First Brillouin Zone is illustrated in Fig. 4. Shown are the lowest three out-of-plane modes (obtained from simulations using Timoshenko beam elements). Different modes are indicated by different colors. The modes span all frequencies from $\bar{f} = 0$ to $\bar{f} = 0.223$, so that no full bandgap exists in this frequency range.

For the four representative frequencies of $\bar{f} = \{0.05, 0.1, 0.15, 0.2\}$, Fig. 5 illustrates the numerically predicted isofrequency contours of the dispersion relations (i.e., slices through the dispersion surfaces at the four given frequencies, as shown in Fig. 4) together with the power spectral density from experiments. Numerical predictions are shown as lines, experimental data as background contours, from which the relevant modes become visible as intensity maxima. Overall, experiment and simulation are in excellent agreement: for all three modes, the power spectral density exhibits largest amplitudes in $\boldsymbol{k}$-space exactly where the modes

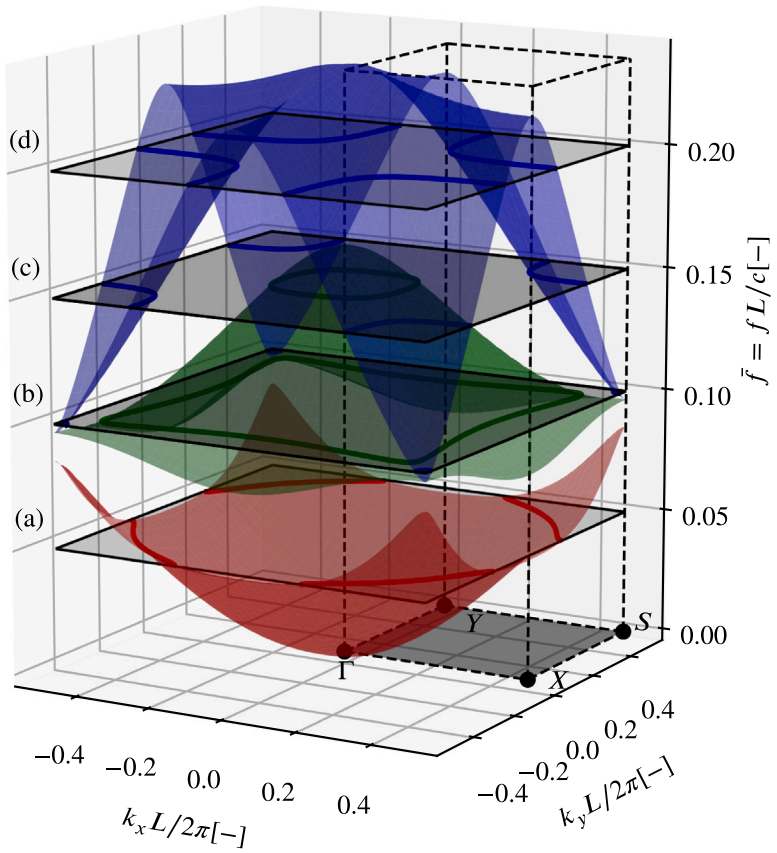

Fig. 4. Dispersion surfaces $\bar{f}(\boldsymbol{k}) = \omega(\boldsymbol{k})L/(2\pi c)$ of the three lowest out-of-plane modes in a square lattice (i. e., $\gamma = 1$) in the FBZ. Each mode is assigned a distinct color. We indicate four horizontal iso-frequency slices at (a) $\bar{f} = 0.05$, (b) $\bar{f} = 0.1$, (c) $\bar{f} = 0.15$, and (d) $\bar{f} = 0.2$. The high-symmetry path Γ-X-S-Y is indicated by dashed lines. All dispersion surfaces were calculated using Timoshenko beam elements.

are expected. A complete scan through the dispersion surfaces across the full investigated frequency range, comparing theoretical predictions to experimental data, is available in Supplementary Video 1.

In addition to slicing through $\boldsymbol{k}$-space, we cut through frequency space following the classical high-symmetry $\boldsymbol{k}$-path for rectangular lattices (Γ-X-S-Y, indicated by the dashed box in Fig. 4). Numerical and experimental results are compared in Fig. 6. Besides the numerical predictions based on Timoshenko beam theory (solid lines), we here include the results of a fully discretized finite element model using solid tetrahedral elements (indicated by triangular markers). Again, an excellent agreement between experimental and numerical results is confirmed, as already seen from the slices through $\boldsymbol{k}$-space. While the fully resolved FE simulations are in almost perfect agreement with experiments, the predictions based on Timoshenko beam theory tend to underestimate $\bar{f}$ for given $\boldsymbol{k}$. These deviations are negligible for low frequencies but can become significant with increasing frequency $\bar{f}$. This observation is in line with earlier work of Hutchinson (1981), who found that the chosen shear correction factor (19) tends to underestimate the natural frequency of beams. In addition to this quantitative discrepancy between the models, we note a qualitative difference for higher frequencies, manifesting in a noticeably different gradient of the third mode for $\bar{f} > 0.225$. This will become important when interpreting the group velocity plots later.

For completeness and for an intuitive representation of the directionality of wave motion, we also compute a group velocity map for the square lattice by differentiating the dispersion surfaces in Fig. 4 and including all modes that have relevance for $\bar{f} \leq 0.25$ (which includes the lowest four modes). The resulting group velocity map is shown in Fig. 7, highlighting the group velocity (by the color code) for any orientation in the 2D plane as well as for any frequency up to $\bar{f} = 0.25$ (rays in the polar plot correspond to constant orientations, while a circle of constant radius corresponds to a fixed frequency). By symmetry, plots for the square lattice are invariant to rotations of 90°, so that the full map (on the left) can be constructed from only a single quadrant (shown on the right for each of the four lowest modes). When two modes overlap in a frequency band, the wave may travel with both modes at different speeds. In experiments, the faster mode will arrive first and is hence observed as the effective group velocity. We therefore combine the information of all relevant modes up to the cut-off frequency $\bar{f} = 0.25$ by presenting the *maximum* group velocity at each point, which is shown on the left in Fig. 7. This group velocity map admits an intuitive understanding of the effective transient wave dispersion in the square lattice for a given direction and frequency. For example, when waves move in the vertical direction (under 90° and 270°), the strong differences in color at different frequencies imply significantly different speeds at which energy

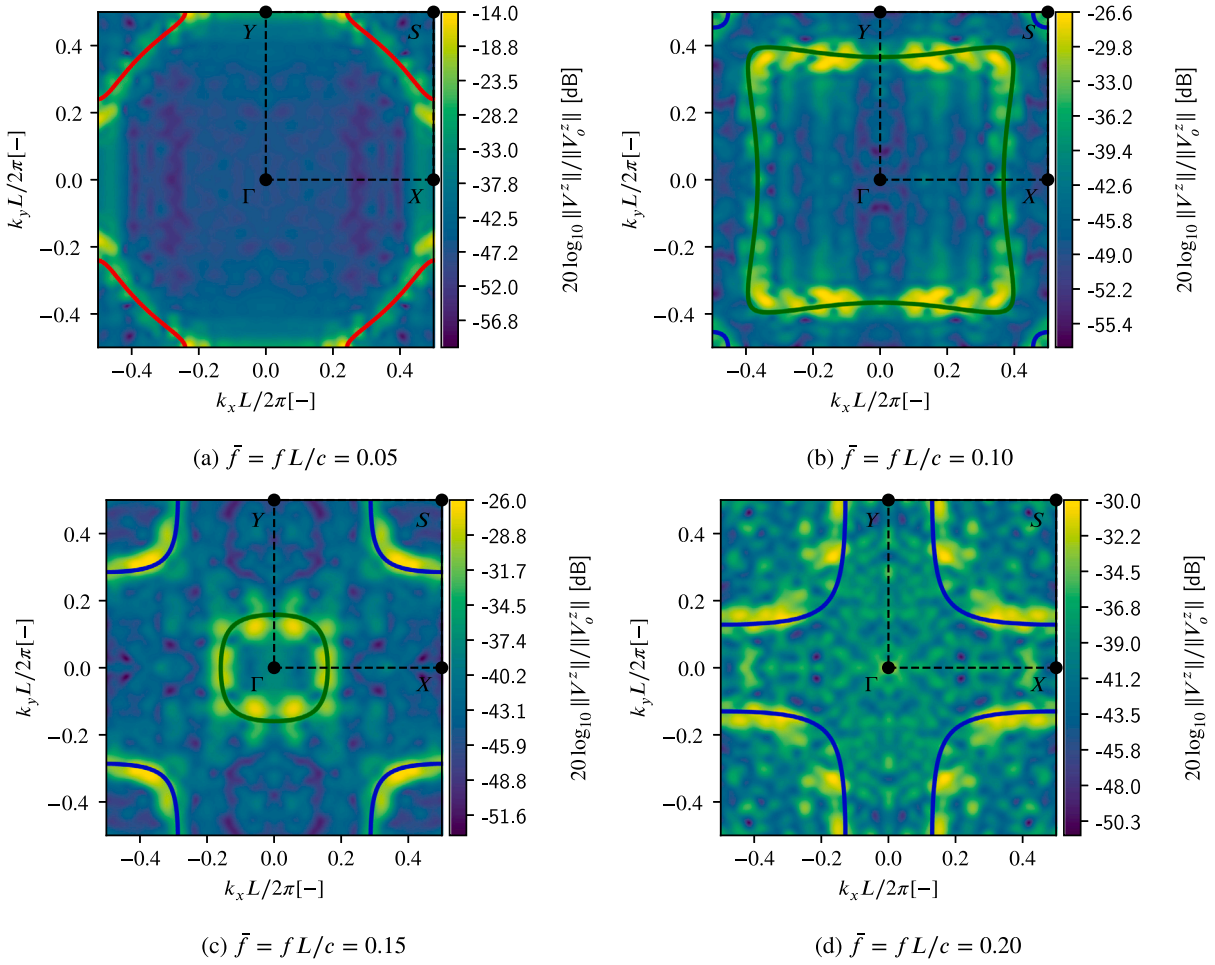

Fig. 5. Isofrequency contours of the dispersion surfaces of the square lattice with an aspect ratio of $\gamma = 1$. Red, green, and blue lines indicate, respectively, the first, second, and third mode, as calculated from Timoshenko beam theory and presented in Fig. 4. The background color shows the experimentally determined power spectral density in a finite periodic square lattice.

flows during wave motion (e.g., compare the low group velocity at $\bar{f} = 0.05$ to the one at $\bar{f} = 0.175$). In the long-wavelength limit of low frequencies, the group velocity is isotropic and waves are expected to spread radially. With increasing frequency, directional wave dispersion becomes apparent from the direction-dependent group velocity – leading to strong anisotropy in wave motion, despite the absence of bandgaps (Zelhofer and Kochmann, 2017; Rosi and Auffray, 2016).

5.2. Rectangular lattice

As a second example, we analyze the rectangular lattice with an aspect ratio of $\gamma = 2$. Applying the same numerical and experimental protocols as before yields the four isofrequency slices through $\boldsymbol{k}$-space shown in Fig. 8. For frequencies $\bar{f} \leq 0.15$, we observe five out-of-plane modes indicated by different colors. Like for the square lattice, the numerical predictions based on Timoshenko beam theory and the peaks in power spectral density from experiments agree well for the four shown slices. Fig. 9 shows the analogous information along the high-symmetry $\boldsymbol{k}$-path Γ-X-S-Y-Γ for $\bar{f} \leq 0.25$.

In contrast to the square lattice with three relevant modes, at least five modes are relevant for wave dispersion in the rectangular lattice with an aspect ratio of $\gamma = 2$. As before, Fig. 9 shows excellent agreement between model predictions and experiments for the lowest three modes at frequencies $\bar{f} \leq 0.1$. For higher modes and frequencies, however, we observe increasing disagreement. First, the results based on Timoshenko beam theory show increasing deviations from experiments, which can in part be attributed to the shear correction factor (Hutchinson, 1981), as discussed before. In addition, some modes are only visible for a fraction of the high-symmetry $\boldsymbol{k}$-path – both in experiments and in the numerical results based on fully-resolved FE. This is a consequence of only capturing out-of-plane modes with our analysis. In fact, the location along the $\boldsymbol{k}$-path where a mode disappears depends on the threshold defined to differentiate between in-plane and out-of-plane modes (Eq. (16)). Hence, a disappearing mode indicates that the mode transitions from out-of-plane to in-plane. The results based on Timoshenko beam theory do not capture this behavior, as

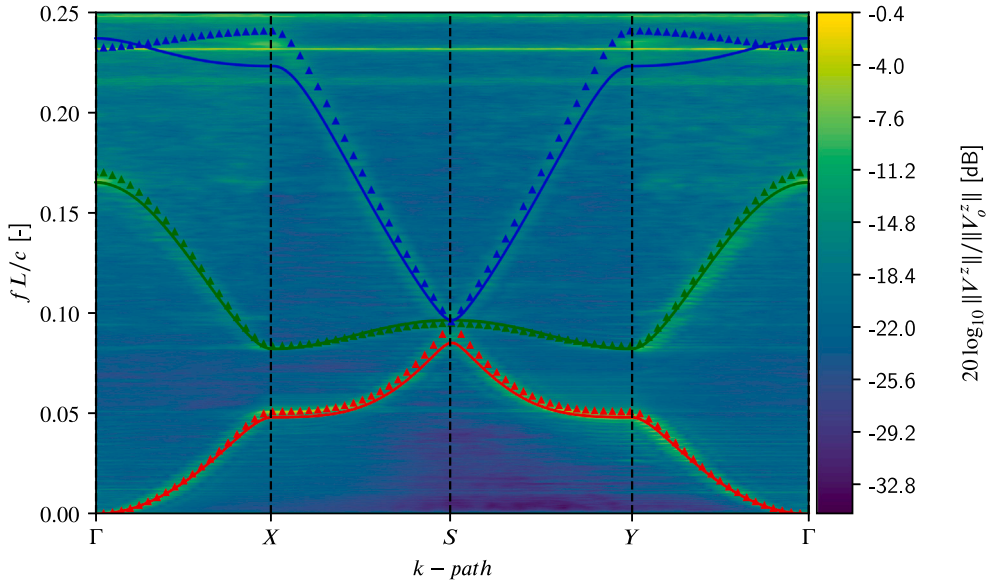

Fig. 6. Dispersion relations along the high-symmetry path Γ-X-S-Y-Γ of the square unit cell with $\gamma = 1$. All out-of plane modes up to $f\,L/c < 0.25$ are shown. Solid lines show the computed dispersion relations based on Timoshenko beam elements, triangular markers were obtained from solid (constant-strain triangular) finite elements. The background color code indicates the experimentally determined power spectral density.

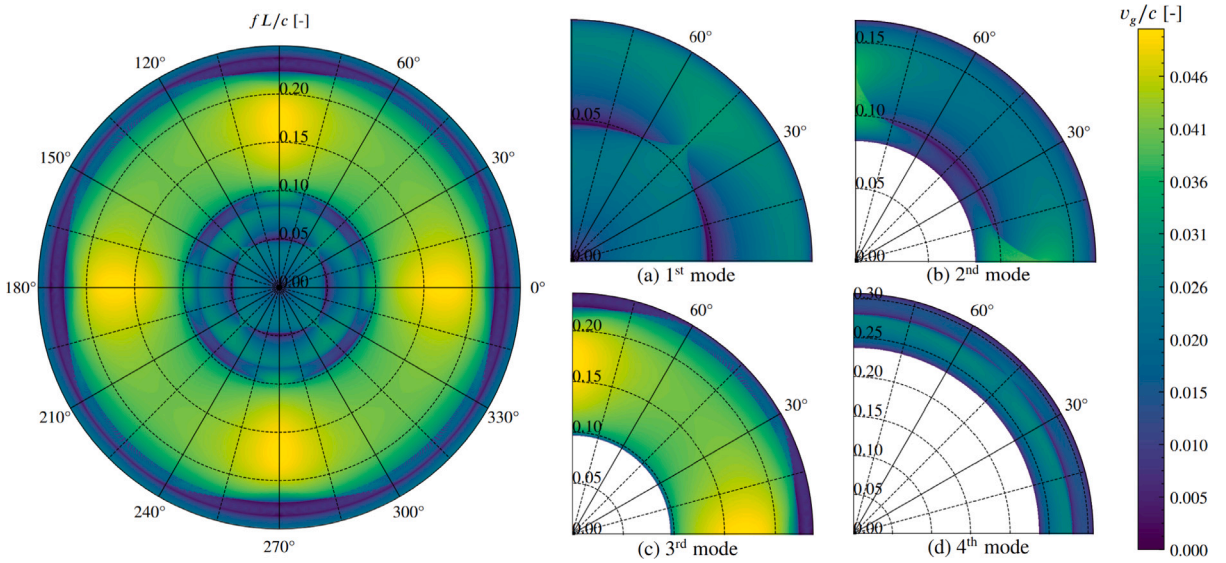

Fig. 7. Group velocity map for the square lattice with an aspect ratio of $\gamma = 1$ for all frequencies $f\,L/c < 0.25$, which is constructed from the lowest four out-of-plane modes (a-d). All plots are based on Timoshenko beam theory, showing the maximum group velocity for each combination of frequency and direction.

the affected modes continue as out-of-plane modes (but thereby miss to capture physical reality, as the experiments mainly confirm the fully-resolved FE predictions).

A group velocity plot for the FBZ (acknowledging symmetry and presenting only the first quadrant) is shown in Fig. 15(f). This group velocity plot includes white regions, which are frequency bands in which none of the involved dispersion surfaces offers a mode for a wave to travel at given frequency and direction. If a white domain extends around the entire polar plot (i.e., appears for all angles), then it represents a full stop band. For the rectangular lattice with $\gamma = 2$, four separated bandgaps appear for $\bar{f} < 0.25$, none presenting a full bandgap but all extending over ranges of directions. These "*directional stop bands*" imply no wave motion in particular directions at the respective frequencies. For example, waves traveling in the vertical direction (at 90°) are attenuated in two frequency bands: one appearing at low frequencies (around $\hat{f} = 0.02$) and a second at higher frequencies (around $\hat{f} = 0.17$), as seen in Fig. 15(f). In addition, the plotted range of frequencies overall shows strong differences in group velocity.

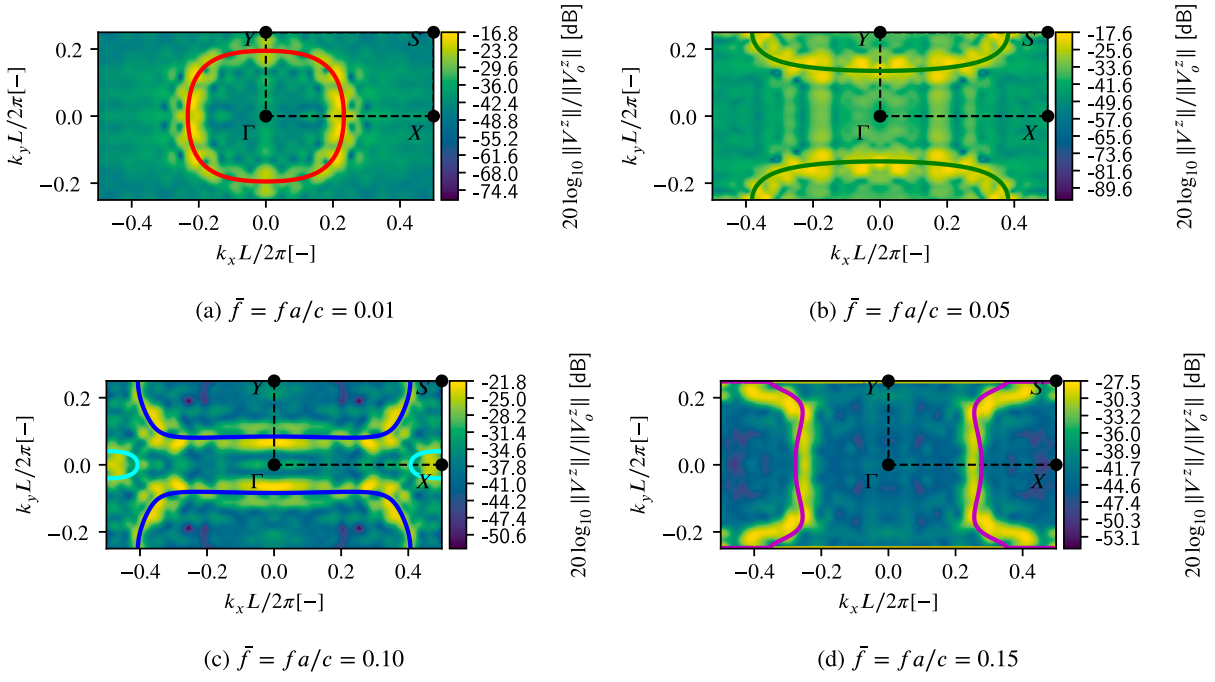

Fig. 8. Isofrequency contours of the dispersion surfaces of the rectangular lattice with aspect ratio $\gamma = 2$. Differently colored lines indicate the different modes, as calculated from Timoshenko beam theory. The background color shows the experimentally determined power spectral density in a finite periodic square lattice.

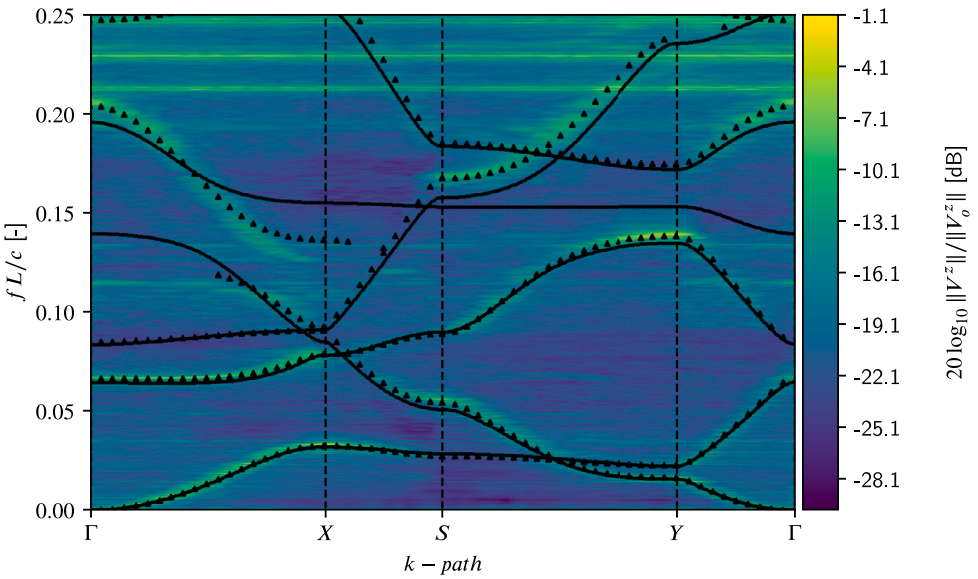

Fig. 9. Dispersion relations along the high-symmetry path Γ-X-S-Y-Γ of the rectangular unit cell with aspect ratio $\gamma = 2.0$. Solid lines and triangles represent, respectively, results obtained from Timoshenko beam theory and fully resolved FE analysis. The experimental signal strength is shown by the background color scheme.

For the discussion of spatially graded lattices in the following, Figs. 14 and 15 in Appendix B illustrate the group velocity plots for various rectangular unit cells of different aspect ratios γ, clearly showing how bandgaps and the associate directionality of wave motion change with aspect ratio γ.

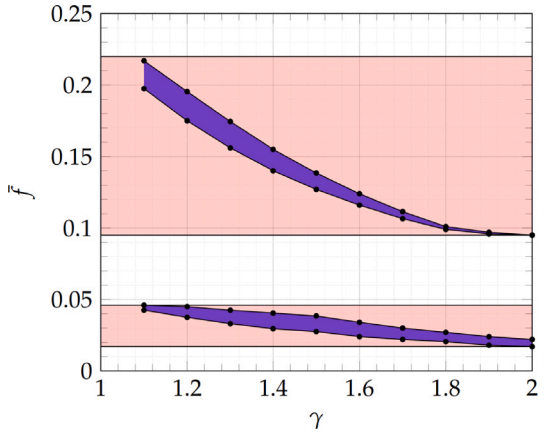

Fig. 10. Variation of the frequency interval (in blue) covered by the lowest two directional stop bands in the vertical direction (under an angle of 90°) versus the unit cell aspect ratio γ of rectangular unit cells. When a wave experiences all of those bandgaps in a spatially graded lattice, the resulting wave motion is expected to be attenuated by all those bandgaps, resulting in the effective, combined stop bands highlighted in red.

5.3. Spatially graded lattice

Having seen the influence of the unit cell aspect ratio γ on the wave dispersion in periodic lattices, we now utilize that directionality information (contained in the group velocity maps of Figs. 14 and 15 in Appendix C) to predict the effective wave propagation in a spatially graded lattice.

We consider a truss lattice that is spatially graded with a changing aspect ratio γ in the vertical direction, as shown in Fig. 2. Consequently, waves moving in the vertical direction experience all aspect ratios contained in the lattice, which is why we are primarily concerned with directional stop bands under an angle of $\theta = 90°$ (or, equivalently, $\theta = 270°$). Identifying all stop bands in this direction from the group velocity maps in Figs. 14 and 15 in Appendix C results in the summary plot in Fig. 10, which highlights in blue, for each value of γ, the frequency range covered by the lowest two directional stop bands in the 90°-direction. These stop bands are continuously varying with γ. As a consequence, in the spatially varying lattice of Fig. 2, where the aspect ratio changes gradually from $\gamma = 1$ at the origin to $\gamma = 2$ at the top and bottom, we expect waves traveling in the vertical direction to experience the superposition of all those bandgaps. This results in an effective bandgap of the graded lattice spanning the all frequency ranges highlighted in red in Fig. 10, which were obtained by combining the local bandgaps. Of course, this conclusion is based on the assumption that the *local* dispersion relations (obtained from Bloch wave analysis on an infinite periodic lattice) are meaningful also in a spatially graded lattice. This is usually the case if the spatial grading is sufficiently smooth (Dorn and Kochmann, 2022, 2023a), so that the wave locally still interacts with an approximately periodic lattice.

To demonstrate the combined attenuation effect, we performed transient simulations on the spatially graded lattice. The resulting maximum wave velocities during simulations are summarized in Figs. 16 and 17 in Appendix C. For each frequency, the onset of the theoretical combined stop band is indicated by a dashed line. (Simulation end times were chosen such that boundary reflections are avoided and only the transient wave is visible.) Results illustrate that waves are indeed attenuated in the vertical direction approximately where expected from the local dispersion relations.

To obtain experimental data for comparison, the center node of a spatially graded lattice was excited at different harmonic excitation frequencies inside and outside of the red domains in Fig. 10. Fully-resolved particle velocity measurements (as detailed in Section 3) were conducted. As it is difficult to apply a harmonic excitation with a single frequency due to the transient nature in the ramp up of any excitation, we applied the same frequency chirps shown in Fig. 12 (a snapshot of the particle velocity at $\bar{t} = 150$ is shown in Fig. 13(c)). As the Brillouin zone – unlike for the previously studied periodic lattices – loses its meaning for the graded lattice, we perform the Fourier transform only in time and present the power spectral density along the vertical y-axis.

The thus-obtained data, summarized via the spectral intensity in Fig. 11, shows that the transient wave is indeed strongly attenuated in the expected regions (the theoretically predicted local stop bands and the resulting effective stop band in the vertical direction of wave motion are included as shaded and hatched regions, respectively). Hence, the graded lattice does effectively combine the directional local stop bands of the different rectangular unit cells into an effective stop band over a broad frequency range. Consequently, the energy of the input chirp focuses in a frequency band between the two effective stop bands (the resulting wedge in frequency-aspect ratio space is also referred to as *metawedge* in photonics (Tsakmakidis et al., 2007)). In this domain we observe a growth in signal strength by several orders of magnitude, which effectively demonstrates ultrasonic rainbow trapping (Tsakmakidis et al., 2007) of mechanical out-of-plane waves in the spatially graded truss lattice. Trainiti et al. (2017) observed analogous behavior when studying in-plane waves in a 3D-printed polymeric structure with graded undulations, whereas Aguzzi et al. (2022) added point masses to add grading to a structure, resulting in wave filtering. By contrast, the metallic truss lattice samples used here are easy to fabricate and to deploy. They come with minimal material-intrinsic damping, which admits approximately linear elastic wave motion and excellent agreement with numerical predictions of the wave attenuation

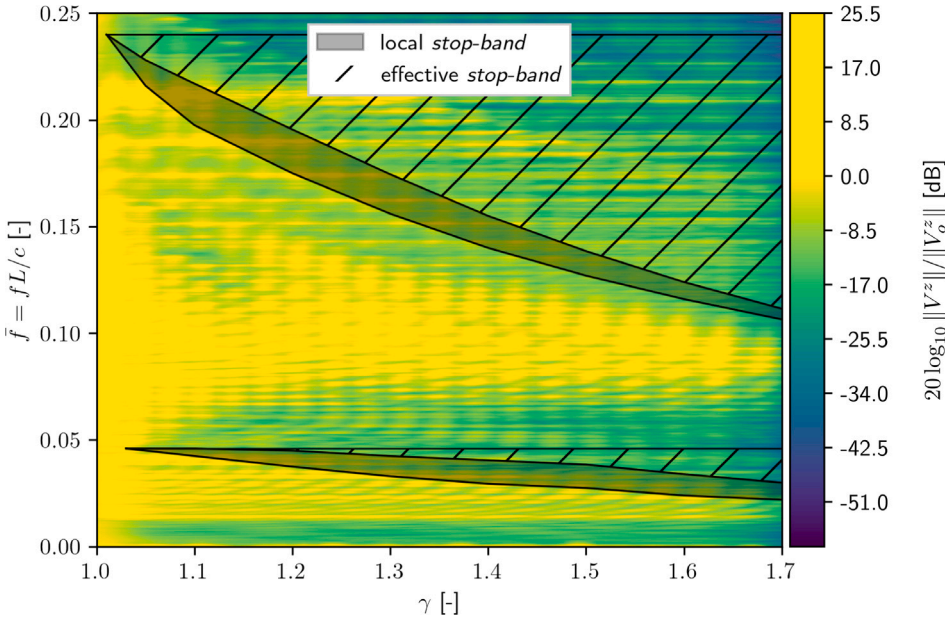

Fig. 11. Experiment vs. theory: wave attenuation in a spatially graded lattice with varying aspect ratio γ of the rectangular unit cell in the vertical y-direction (Fig. 2). The wave attenuation is obtained by normalizing the time Fourier amplitudes at each y-location with the excitation signal at the origin. The theoretically expected stop bands from Bloch wave analysis are overlaid as shaded regions, resulting in the combined, effective stop bands shown by the hatched regions. The wave propagation is attenuated at different γ-values in agreement with the local stop bands. Overall, two effective bandgaps are visible, so that waves propagate primarily in the two (yellow) wedges outside those frequency ranges.

in the graded structure (see Appendix C). We further focused on out-of-plane vibrations, which present a frequent load case in, e.g., micro- and nano-electromechanical systems and operate generally at lower frequencies than in-plane modes, which is beneficial for miniaturization.

6. Conclusion

Truss lattices are excellent mechanical wave guides, whose dispersion relations can be controlled through the unit cell architecture and utilized to purposefully attenuate or steer stress waves. Our experiments on laser-cut 2D metallic trusses with varying unit cell geometries, characterized in-situ by laser Doppler velocimetry and combined with a Fourier-based data analysis protocol, allowed for the experimental measurement of complete dispersion surfaces of the lowest modes – going beyond many prior studies that were limited to verifying the existence of bandgaps through confirming reduced wave transmissibility or focusing on particular paths in $\boldsymbol{k}$-space. Moreover, experimental findings were shown to be in excellent agreement with finite element predictions based on Bloch wave analysis. Our experiments confirmed that, while Timoshenko beam theory is suitable for the lowest few modes and at low frequencies, it fails to accurately predict the dispersion relations at higher frequencies – unlike fully-resolved finite element simulations based on solid elements, which provide accurate predictions in this study. Going beyond periodic trusses, we analyzed a spatially graded design, in which the unit cell's aspect ratio continuously changes to create a phononic bandgap across a wide frequency range. Experiments on a graded sample confirmed the predictions made by "stacking" the local dispersion relations of individual unit cells, thus demonstrating the validity of the (locally periodic) dispersion relations if the spatial grading is sufficiently smooth. The two observed wedges forced the wave energy to focus in a frequency band between the wedges, resulting in strongly increased amplitudes observed within this frequency band. This proves the emergence of 'broadband rainbow trapping' of mechanical waves in truss lattices undergoing out-of-plane vibrational motion. While all effects can be scaled to different frequency domains (the reported phenomena are scale-independent), experiments were conducted at ultrasound frequencies with potential applications, e.g., in the medical sector. Moreover, the out-of-plane mode of excitation – along with the simple unit cell design – bears potential for miniaturization as well as for applications from wave guidance and energy harvesting to vibration control in micro- and nanomechanical systems.

CRediT authorship contribution statement

Bastian Telgen: Writing – review & editing, Writing – original draft, Visualization, Validation, Software, Methodology, Investigation, Formal analysis, Data curation, Conceptualization. **Vignesh Kannan:** Writing – original draft, Visualization, Validation, Software, Methodology, Investigation, Data curation, Conceptualization. **Jean-Charles Bail:** Software, Methodology, Investigation, Formal analysis. **Charles Dorn:** Writing – original draft, Software, Methodology, Investigation, Data curation. **Hannah**

Niese: Methodology, Investigation. **Dennis M. Kochmann:** Writing – review & editing, Supervision, Methodology, Investigation, Conceptualization.

Declaration of competing interest

The authors declare that they have no known competing financial interests or personal relationships that could have appeared to influence the work reported in this paper.

Data availability

Data will be made available on request.

Acknowledgment

C.D. was supported by an ETH Zurich Postdoctoral Fellowship.

Appendix A. Frequency chirp signals and raw velocity field data

This appendix illustrates representative experimental data. Fig. 12 presents the linear frequency chirp signal applied to samples and measured at the center node of the lattice, shown both in the time domain and in the frequency domain. Three different frequency chirps were used to span a wide frequency range in experiments, thus covering the full range of frequencies of interest. To illustrate the measured response of the truss lattice, Fig. 13 shows the raw velocity field data obtained from three different 2D truss lattices: a square lattice with aspect ratio $\gamma = 1$, a rectangular lattice with an aspect ratio of $\gamma = 2$, and the spatially graded lattice of Fig. 2, whose aspect ratio varies between $\gamma = 1$ and $\gamma = 2$ from the center towards the top and bottom. All data were taken at $t = 150$ μs after the onset of excitation; the raw out-of-plane velocity data are shown by the color code.

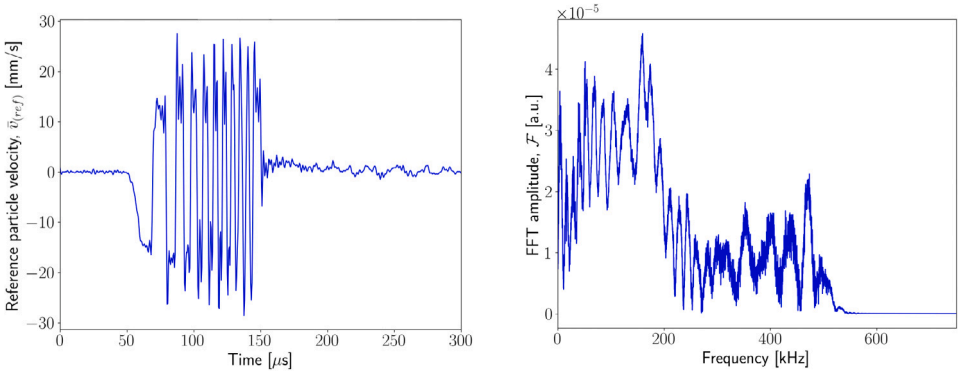

Fig. 12. Linear frequency chirp signal measured at the center node in (a) the time domain and (b) the frequency domain. Three different frequency chirps were used to span a wide frequency domain.

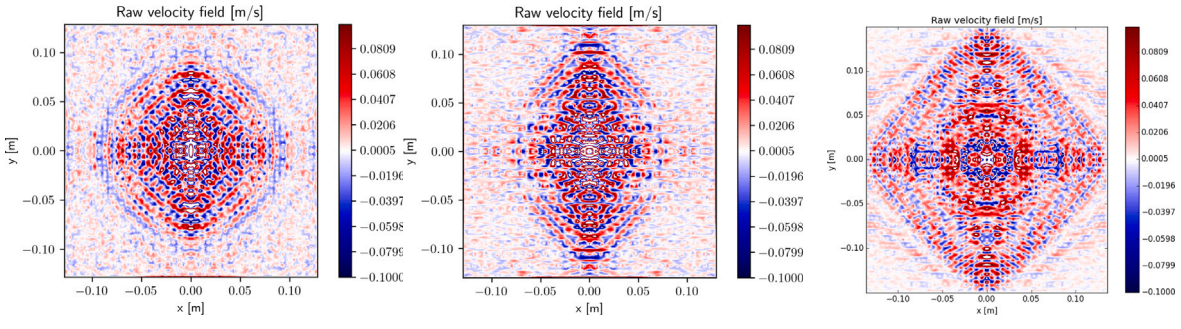

Fig. 13. Raw velocity fields at $t = 150$ μs for periodic truss lattices with aspect ratios (a) $\gamma = 1$ and (b) $\gamma = 2$, and (c) the spatially graded lattice with γ ranging from center to top and bottom from 1 to 2, respectively.

Appendix B. Group velocity of out-of-plane modes for $1.0 \geq \gamma \geq 2.0$

Group velocity maps of the out-of-plane modes for rectangular unit cells with aspect ratios $1.0 \leq \gamma \leq 2.0$ are shown in Figs. 14 and 15.

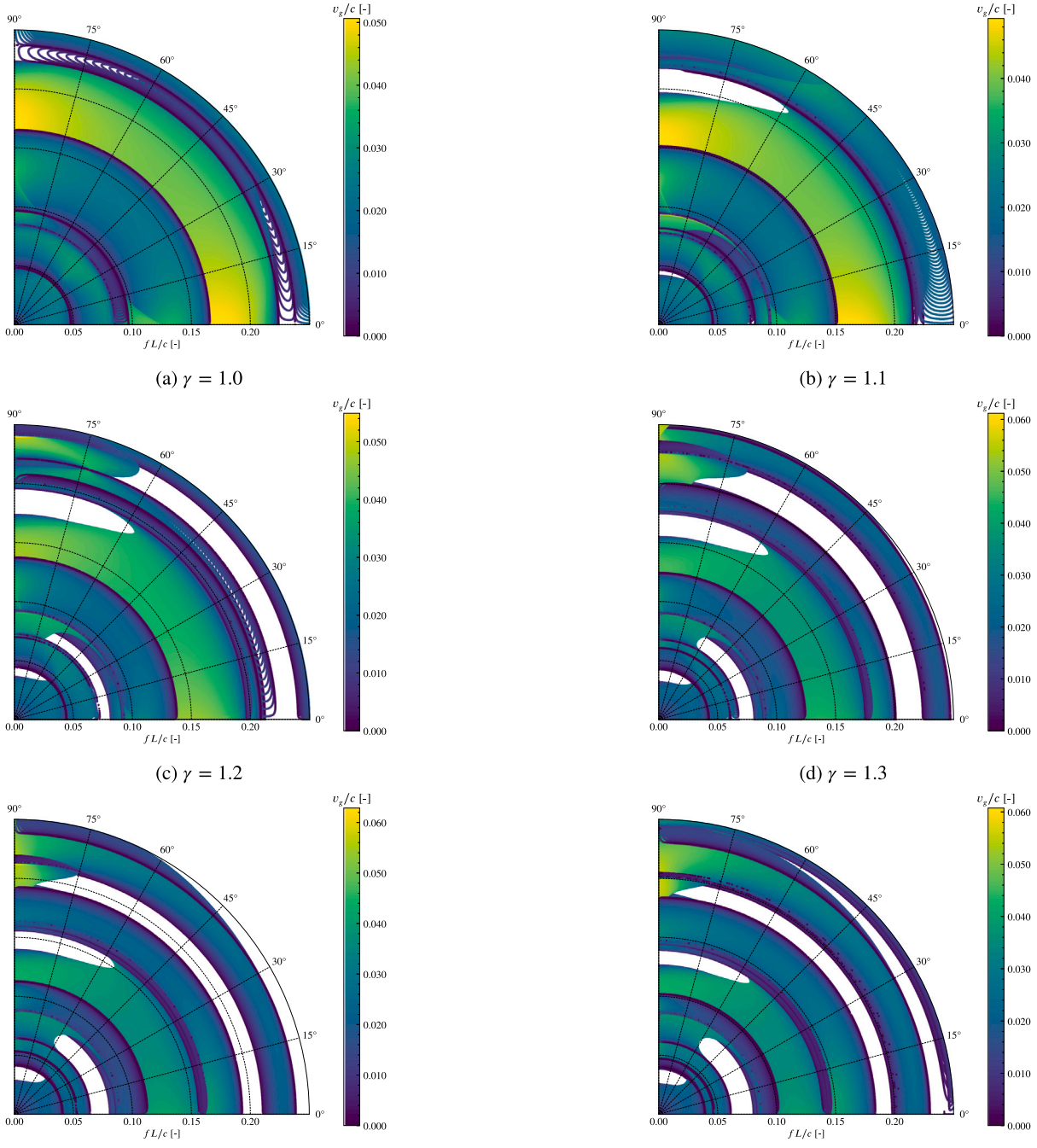

(a) $\gamma = 1.0$ (b) $\gamma = 1.1$

(c) $\gamma = 1.2$ (d) $\gamma = 1.3$

(e) $\gamma = 1.4$ (f) $\gamma = 1.5$

Fig. 14. Group velocity maps of the out-of-plane modes for rectangular unit cells with aspect ratios $1.0 \leq \gamma \leq 1.5$.

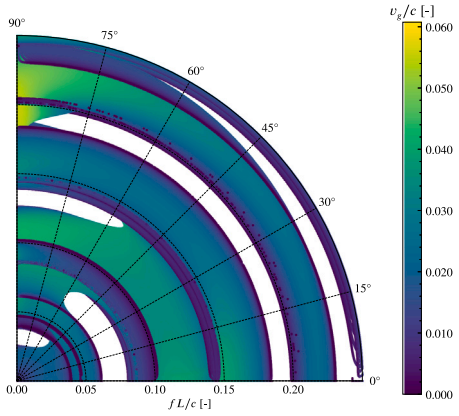

(a) $\gamma = 1.5$

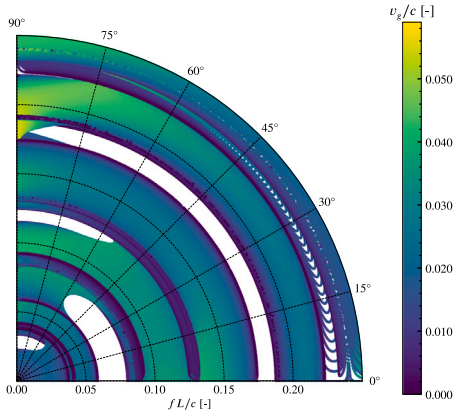

(b) $\gamma = 1.6$

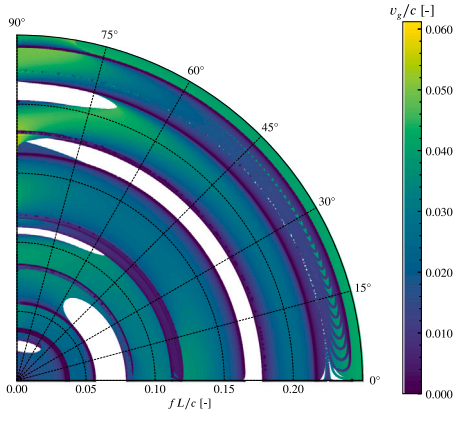

(c) $\gamma = 1.7$

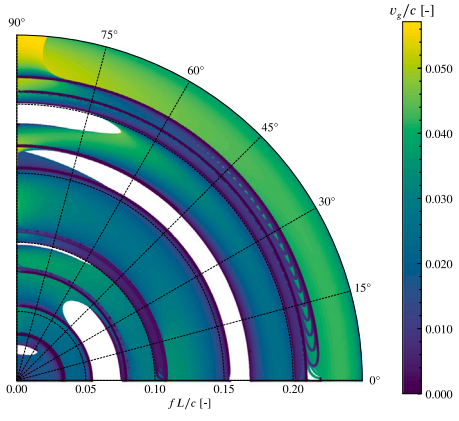

(d) $\gamma = 1.8$

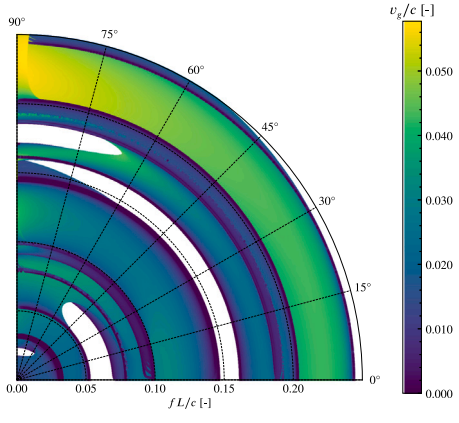

(e) $\gamma = 1.9$

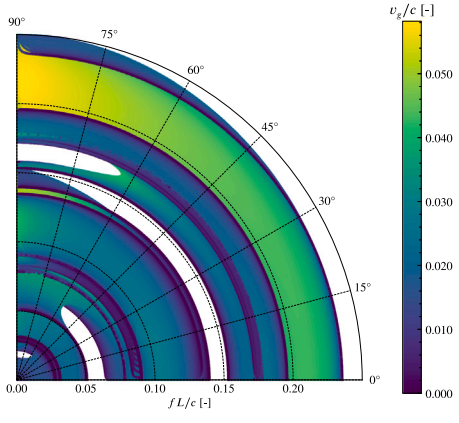

(f) $\gamma = 2.0$

Fig. 15. Group velocity maps of the out-of-plane modes for rectangular unit cells with aspect ratios $1.5 \leq \gamma \leq 2.0$.

Appendix C. Maximum out-of-plane velocity in a square lattice

Profiles of the maximum out-of-plane velocity in a spatially graded lattice, as obtained from simulations based on Timoshenko beam elements are shown in Figs. 16 and 17. Red boxes indicate those unit cells that fall into a local stop band, based on Bloch theory predictions.

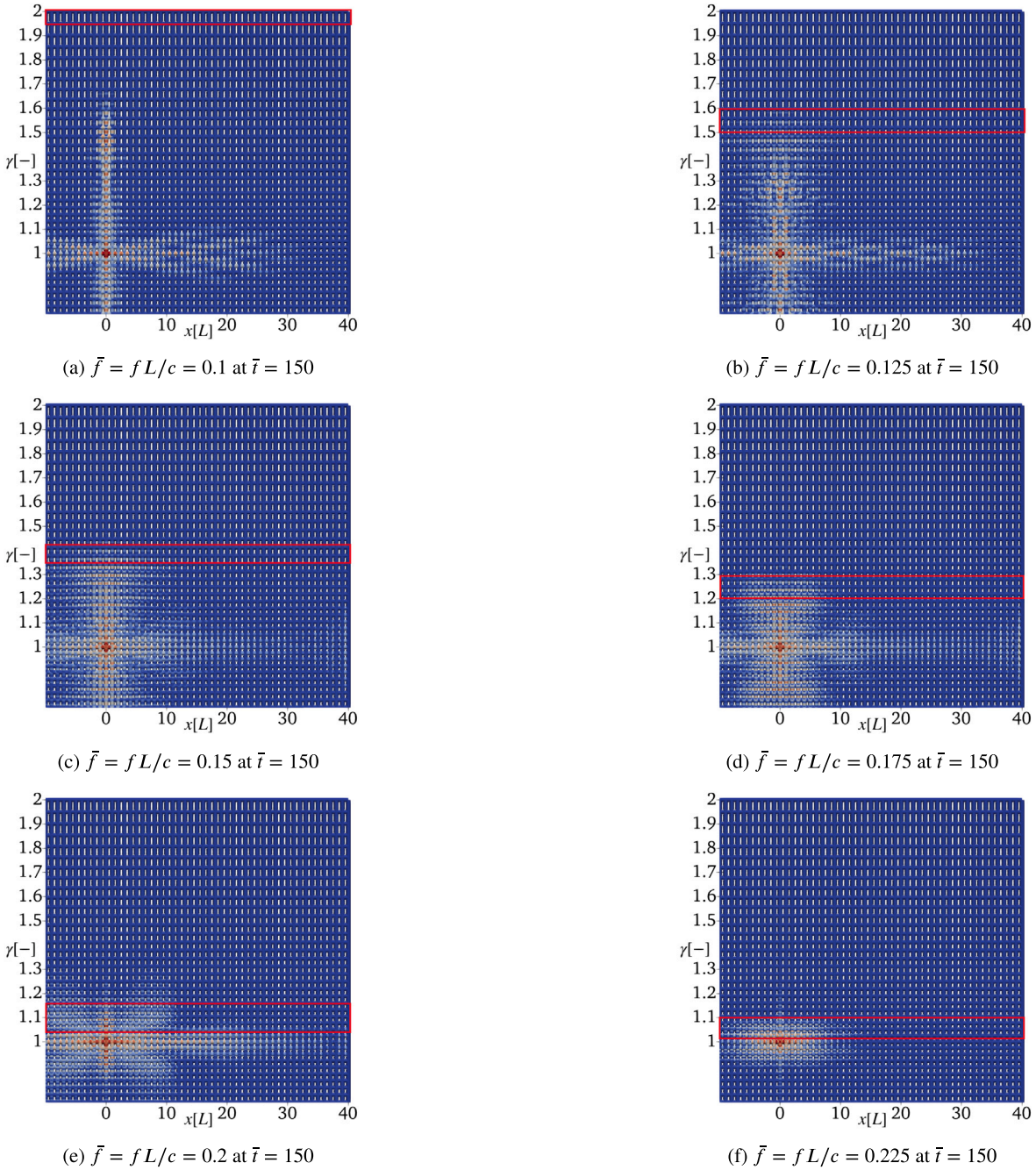

(a) $\bar{f} = fL/c = 0.1$ at $\bar{t} = 150$

(b) $\bar{f} = fL/c = 0.125$ at $\bar{t} = 150$

(c) $\bar{f} = fL/c = 0.15$ at $\bar{t} = 150$

(d) $\bar{f} = fL/c = 0.175$ at $\bar{t} = 150$

(e) $\bar{f} = fL/c = 0.2$ at $\bar{t} = 150$

(f) $\bar{f} = fL/c = 0.225$ at $\bar{t} = 150$

Fig. 16. Maximum out-of-plane velocity in a spatially graded lattice, as obtained from simulations based on Timoshenko beam elements. Red boxes indicate those unit cells that fall into a local stop band, based on Bloch theory predictions.

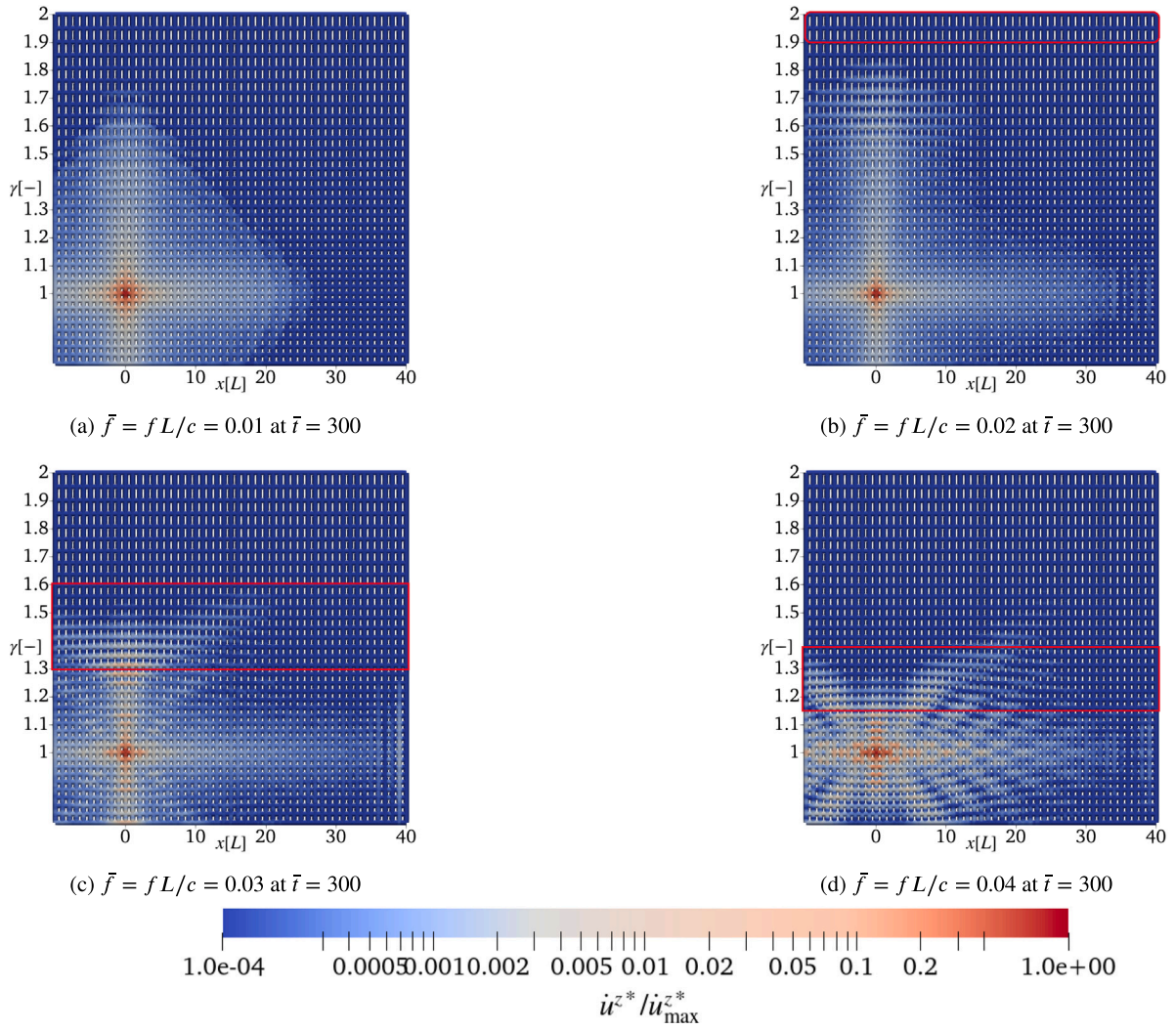

Fig. 17. Maximum out-of-plane velocity in a spatially graded lattice, as obtained from simulations based on Timoshenko beam elements. Red boxes indicate those unit cells that fall into a local stop band, based on Bloch theory predictions.

Appendix D. Supplementary data

Supplementary material related to this article can be found online at https://doi.org/10.1016/j.jmps.2024.105762.

References

Aguzzi, G., Kanellopoulos, C., Wiltshaw, R., Craster, R.V., Chatzi, E.N., Colombi, A., 2022. Octet lattice-based plate for elastic wave control. Sci. Rep. 12, 1088. http://dx.doi.org/10.1038/s41598-022-04900-0, URL https://www.nature.com/articles/s41598-022-04900-0. number: 1 Publisher: Nature Publishing Group.

Bilal, O.R., Hussein, M.I., 2011. Ultrawide phononic band gap for combined in-plane and out-of-plane waves. Phys. Rev. E 84, http://dx.doi.org/10.1103/PhysRevE.84.065701, URL http://arxiv.org/abs/1111.1457. arXiv:1111.1457.

Bilal, O.R., Yee, C.H., Rys, J., Schumacher, C., Daraio, C., 2021. Experimental realization of phonon demultiplexing in three-dimensions. Appl. Phys. Lett. 118, 091901. http://dx.doi.org/10.1063/5.0030830, URL https://aip.scitation.org/doi/full/10.1063/5.0030830, publisher: American Institute of Physics.

Bloch, F., 1929. Über die quantenmechanik der elektronen in kristallgittern. Z. Phys. 52, 555–600. http://dx.doi.org/10.1007/BF01339455.

Bravais, A., 1850. Mémoire sur les systèmes formés par des points distribués régulièrement sur un plan ou dans l'espace. J. École Polytechnique 19, 1–128, URL https://gallica.bnf.fr/ark:/12148/bpt6k96124j.

Brillouin, L., 1946. Wave Propagation in Periodic Structures. Dover Publications, Inc., New York, N.Y.

Casadei, F., Rimoli, J.J., 2013. Anisotropy-induced broadband stress wave steering in periodic lattices. Int. J. Solids Struct. 50, 1402–1414. http://dx.doi.org/10.1016/j.ijsolstr.2013.01.015, URL https://www.sciencedirect.com/science/article/pii/S0020768313000309.

Chang, Z., Hu, G., 2012. Elastic wave omnidirectional absorbers designed by transformation method. Appl. Phys. Lett. 101.

Chen, H., Chan, C.T., 2010. Acoustic cloaking and transformation acoustics. J. Phys. D: Appl. Phys. 43, 113001.

Chen, Y., Hu, J., Huang, G., 2016. A design of active elastic metamaterials for control of flexural waves using the transformation method. J. Intell. Mater. Syst. Struct. 27, 1337–1347.

Collet, M., Ouisse, M., Ruzzene, M., Ichchou, M.N., 2011. Floquet–Bloch decomposition for the computation of dispersion of two-dimensional periodic, damped mechanical systems. Int. J. Solids Struct. 48, 2837–2848. http://dx.doi.org/10.1016/j.ijsolstr.2011.06.002, URL https://www.sciencedirect.com/science/article/pii/S0020768311002125.

Colombi, A., Colquitt, D., Roux, P., Guenneau, S., Craster, R.V., 2016. A seismic metamaterial: The resonant metawedge. Sci. Rep. 6, 27717. http://dx.doi.org/10.1038/srep27717, URL https://www.nature.com/articles/srep27717, number: 1 Publisher: Nature Publishing Group.

Cowper, G.R., 1966. The shear coefficient in Timoshenko's beam theory. J. Appl. Mech. 33, 335–340. http://dx.doi.org/10.1115/1.3625046.

D'Alessandro, L., Belloni, E., Ardito, R., Corigliano, A., Braghin, F., 2016. Modeling and experimental verification of an ultra-wide bandgap in 3D phononic crystal. Appl. Phys. Lett. 109, 221907. http://dx.doi.org/10.1063/1.4971290, URL https://aip.scitation.org/doi/full/10.1063/1.4971290. publisher: American Institute of Physics.

De Ponti, J.M., Colombi, A., Riva, E., Ardito, R., Braghin, F., Corigliano, A., Craster, R.V., 2020. Experimental investigation of amplification. via a mechanical delay-line, in a rainbow-based metamaterial for energy harvesting. Appl. Phys. Lett. 117.

Dorn, C., Kochmann, D.M., 2022. Ray theory for elastic wave propagation in graded metamaterials. J. Mech. Phys. Solids 168, 105049. http://dx.doi.org/10.1016/j.jmps.2022.105049, URL https://www.sciencedirect.com/science/article/pii/S0022509622002277.

Dorn, C., Kochmann, D.M., 2023a. Conformally graded metamaterials for elastic wave guidance. Extreme Mech. Lett. 65, 102091. http://dx.doi.org/10.1016/j.eml.2023.102091, URL https://www.sciencedirect.com/science/article/pii/S2352431623001372.

Dorn, C., Kochmann, D.M., 2023b. Inverse design of graded phononic materials via ray tracing. J. Appl. Phys. 134, 195103. http://dx.doi.org/10.1063/5.0176704, arXiv:https://pubs.aip.org/aip/jap/article-pdf/doi/10.1063/5.0176704/18211698/195103_1_5.0176704.pdf.

Gonella, S., To, A.C., Liu, W.K., 2009. Interplay between phononic bandgaps and piezoelectric microstructures for energy harvesting. J. Mech. Phys. Solids 57, 621–633. http://dx.doi.org/10.1016/j.jmps.2008.11.002, URL https://www.sciencedirect.com/science/article/pii/S0022509608001919.

Hernandez, V., Roman, J.E., Vidal, V., 2005. SLEPc: A scalable and flexible toolkit for the solution of eigenvalue problems. ACM Trans. Math. Software 31, 351–362. http://dx.doi.org/10.1145/1089014.1089019.

Hussein, M.I., 2009. Reduced bloch mode expansion for periodic media band structure calculations. Proc. R. Soc. Lond. A: Math., Phys. Eng. Sci. 465, 2825–2848. http://dx.doi.org/10.1098/rspa.2008.0471, URL http://rspa.royalsocietypublishing.org/content/465/2109/2825.

Hussein, M.I., Leamy, M.J., Ruzzene, M., 2014. Dynamics of phononic materials and structures: Historical origins, recent progress, and future outlook. Appl. Mech. Rev. 66, http://dx.doi.org/10.1115/1.4026911, 040802–040802.

Hutchinson, J.R., 1981. Transverse vibrations of beams, exact versus approximate solutions. J. Appl. Mech. 48, 923–928. http://dx.doi.org/10.1115/1.3157757.

Joannopoulos, J.D., Johnson, S.G., Winn, J.N., Meade, R.D., 1995. Photonic Crystals: Molding the Flow of Light - Second Edition. Princeton University Press, http://dx.doi.org/10.1515/9781400828241, publication Title: Photonic Crystals. URL https://www.degruyter.com/document/doi/10.1515/9781400828241/html.

Kaneko, T., 1975. On Timoshenko's correction for shear in vibrating beams. J. Phys. D: Appl. Phys. 8, 1927–1936. http://dx.doi.org/10.1088/0022-3727/8/16/003, publisher: IOP Publishing.

Krattiger, D., Hussein, M.I., 2017. Modal reduction of lattice material models. In: Dynamics of Lattice Materials. John Wiley & Sons, Ltd, pp. 199–215. http://dx.doi.org/10.1002/9781118729588.ch9, URL https://onlinelibrary.wiley.com/doi/abs/10.1002/9781118729588.ch9.

Krödel, S., Delpero, T., Bergamini, A., Ermanni, P., Kochmann, D.M., 2014. 3D auxetic microlattices with independently controllable acoustic band gaps and quasi-static elastic moduli. Adv. Eng. Mater. 16, 357–363. http://dx.doi.org/10.1002/adem.201300264, URL https://onlinelibrary.wiley.com/doi/abs/10.1002/adem.201300264.

Kushwaha, M.S., Halevi, P., Dobrzynski, L., Djafari-Rouhani, B., 1993. Acoustic band structure of periodic elastic composites. Phys. Rev. Lett. 71, 2022–2025. http://dx.doi.org/10.1103/PhysRevLett.71.2022, URL http://link.aps.org/doi/10.1103/PhysRevLett.71.2022.

Langley, R.S., Bardell, N.S., Ruivo, H.M., 1997. The response of two-dimensional periodic structures to harmonic point loading: A theoretical and experimental study of a beam grillage. J. Sound Vib. 207, 521–535. http://dx.doi.org/10.1006/jsvi.1997.1154, URL http://www.sciencedirect.com/science/article/pii/S0022460X97911548.

Le, K.C., 1999. Vibrations of Shells and Rods. Springer Berlin Heidelberg, Berlin, Heidelberg, http://dx.doi.org/10.1007/978-3-642-59911-8, oCLC: 851772766.

Li, Y., Baker, E., Reissman, T., Sun, C., Liu, W.K., 2017. Design of mechanical metamaterials for simultaneous vibration isolation and energy harvesting. Appl. Phys. Lett. 111, 251903. http://dx.doi.org/10.1063/1.5008674, URL http://aip.scitation.org/doi/10.1063/1.5008674.

Liu, Z., 2000. Locally resonant sonic materials. Science 289, 1734–1736. http://dx.doi.org/10.1126/science.289.5485.1734, URL http://www.sciencemag.org/cgi/doi/10.1126/science.289.5485.1734.

Mace, B.R., Manconi, E., 2008. Modelling wave propagation in two-dimensional structures using finite element analysis. J. Sound Vib. 318, 884–902. http://dx.doi.org/10.1016/j.jsv.2008.04.039, URL http://www.sciencedirect.com/science/article/pii/S0022460X0800391X.

Matlack, K.H., Bauhofer, A., Krödel, S., Palermo, A., Daraio, C., 2016. Composite 3D-printed metastructures for low-frequency and broadband vibration absorption. Proc. Natl. Acad. Sci. 113, 8386–8390. http://dx.doi.org/10.1073/pnas.1600171113, URL http://www.pnas.org/content/113/30/8386.

Mead, D.J., 1973. A general theory of harmonic wave propagation in linear periodic systems with multiple coupling. J. Sound Vib. 27, 235–260. http://dx.doi.org/10.1016/0022-460X(73)90064-3, URL https://www.sciencedirect.com/science/article/pii/0022460X73900643.

Meza, L.R., Phlipot, G.P., Portela, C.M., Maggi, A., Montemayor, L.C., Comella, A., Kochmann, D.M., Greer, J.R., 2017. Reexamining the mechanical property space of three-dimensional lattice architectures. Acta Mater. 140, 424–432. http://dx.doi.org/10.1016/j.actamat.2017.08.052, URL https://www.sciencedirect.com/science/article/pii/S1359645417307073.

Nassar, H., Chen, Y., Huang, G., 2020. Polar metamaterials: A new outlook on resonance for cloaking applications. Phys. Rev. Lett. 124, 084301.

Pal, R.K., Rimoli, J., Ruzzene, M., 2016. Effect of large deformation pre-loads on the wave properties of hexagonal lattices. Smart Mater. Struct. 25, 054010.

Palermo, A., Marzani, A., 2020. A reduced Bloch operator finite element method for fast calculation of elastic complex band structures. Int. J. Solids Struct. 191-192, 601–613. http://dx.doi.org/10.1016/j.ijsolstr.2019.12.011, URL http://www.sciencedirect.com/science/article/pii/S0020768319304950.

Phani, A.S., Hussein, M.I. (Eds.), 2017. Dynamics of Lattice Materials. John Wiley & Sons, Inc., Chichester, West Sussex, United Kingdom.

Phani, A.S., Woodhouse, J., Fleck, N.A., 2006. Wave propagation in two-dimensional periodic lattices. J. Acoust. Soc. Am. 119, 1995–2005. http://dx.doi.org/10.1121/1.2179748, publisher: Acoustical Society of America. URL https://asa.scitation.org/doi/10.1121/1.2179748.

Portela, C.M., Greer, J.R., Kochmann, D.M., 2018. Impact of node geometry on the effective stiffness of non-slender three-dimensional truss lattice architectures. Extreme Mech. Lett. 22, 138–148. http://dx.doi.org/10.1016/j.eml.2018.06.004, URL https://www.sciencedirect.com/science/article/pii/S2352431618300725.

Rosi, G., Auffray, N., 2016. Anisotropic and dispersive wave propagation within strain-gradient framework. URL http://arxiv.org/abs/1601.07064, arXiv:1601.07064 [cond-mat, physics:physics].

Rumpf, R.C., Pazos, J.J., Digaum, J.L., Kuebler, S.M., 2015. Spatially variant periodic structures in electromagnetics. Phil. Trans. R. Soc. A 373, 20140359. http://dx.doi.org/10.1098/rsta.2014.0359, URL https://royalsocietypublishing.org/doi/10.1098/rsta.2014.0359.

Ruzzene, M., Scarpa, F., Soranna, F., 2003. Wave beaming effects in two-dimensional cellular structures. Smart Mater. Struct. 12, 363–372. http://dx.doi.org/10.1088/0964-1726/12/3/307, publisher: IOP Publishing.

Schaeffer, M., Trainiti, G., Ruzzene, M., 2017. Optical measurement of in-plane waves in mechanical metamaterials through digital image correlation. Sci. Rep. 7, 1–9. http://dx.doi.org/10.1038/srep42437, URL https://www.nature.com/articles/srep42437.

Sigalas, M., Economou, E.N., 1993. Band structure of elastic waves in two dimensional systems. Solid State Commun. 86, 141–143. http://dx.doi.org/10.1016/0038-1098(93)90888-T, URL http://www.sciencedirect.com/science/article/pii/003810989390888T.

Sigalas, M., Kushwaha, M.S., Economou, E.N., Kafesaki, M., Psarobas, I.E., Steurer, W., 2009. Classical vibrational modes in phononic lattices: theory and experiment. Z. für Kristallographie - Crystalline Materials 220, 765–809. http://dx.doi.org/10.1524/zkri.2005.220.9-10.765, URL https://www.degruyter.com/view/j/zkri.2005.220.issue-9-10/zkri.2005.220.9-10.765/zkri.2005.220.9-10.765.xml.

Sigmund, O., 1994. Materials with prescribed constitutive parameters: An inverse homogenization problem. Int. J. Solids Struct. 31, 2313–2329. http://dx.doi.org/10.1016/0020-7683(94)90154-6, URL http://www.sciencedirect.com/science/article/pii/0020768394901546.

Sigmund, O., Jensen, J.S., 2003. Systematic design of phononic band–gap materials and structures by topology optimization. Philos. Trans. R. Soc. Lond. A: Math., Phys. Eng. Sci. 361, 1001–1019. http://dx.doi.org/10.1098/rsta.2003.1177, URL http://rsta.royalsocietypublishing.org/content/361/1806/1001.

Sun, Z., Sun, X., Jia, H., Bi, Y., Yang, J., 2019. Quasi-isotropic underwater acoustic carpet cloak based on latticed pentamode metafluid. Appl. Phys. Lett. 114.

Trainiti, G., Rimoli, J.J., Ruzzene, M., 2017. Optical evaluation of the wave filtering properties of graded undulated lattices. J. Appl. Phys. 123, 091706. http://dx.doi.org/10.1063/1.5011369, URL https://aip.scitation.org/doi/10.1063/1.5011369.

Tsakmakidis, K.L., Boardman, A.D., Hess, O., 2007. 'Trapped rainbow' storage of light in metamaterials. Nature 450, 397–401. http://dx.doi.org/10.1038/nature06285, URL https://www.nature.com/articles/nature06285. number: 7168 Publisher: Nature Publishing Group.

Vasseur, J.O., Deymier, P.A., Frantziskonis, G., Hong, G., Djafari-Rouhani, B., Dobrzynski, L., 1998. Experimental evidence for the existence of absolute acoustic band gaps in two-dimensional periodic composite media. J. Phys.: Condens. Matter. 10, 6051–6064. http://dx.doi.org/10.1088/0953-8984/10/27/006, URL https://iopscience.iop.org/article/10.1088/0953-8984/10/27/006.

Weberndorfer, M., 2020. ae108. URL https://gitlab.ethz.ch/mechanics-and-materials/ae108.

Xie, Y., Fu, Y., Jia, Z., Li, J., Shen, C., Xu, Y., Chen, H., Cummer, S.A., 2018. Acoustic imaging with metamaterial luneburg lenses. Sci. Rep. 8, 16188. http://dx.doi.org/10.1038/s41598-018-34581-7, URL https://www.nature.com/articles/s41598-018-34581-7. number: 1 Publisher: Nature Publishing Group.

Yablonovitch, E., 1987. Inhibited spontaneous emission in solid-state physics and electronics. Phys. Rev. Lett. 58, 2059–2062. http://dx.doi.org/10.1103/PhysRevLett.58.2059, URL https://link.aps.org/doi/10.1103/PhysRevLett.58.2059, publisher: American Physical Society.

Zelhofer, A.J., Kochmann, D.M., 2017. On acoustic wave beaming in two-dimensional structural lattices. International Journal of Solids and Structures 115- 116, 248–269. http://dx.doi.org/10.1016/j.ijsolstr.2017.03.024, URL https://www.sciencedirect.com/science/article/pii/S0020768317301336.

Zhao, L., Laredo, E., Ryan, O., Yazdkhasti, A., Kim, H.T., Ganye, R., Horiuchi, T., Yu, M., 2020. Ultrasound beam steering with flattened acoustic metamaterial Luneburg lens. Appl. Phys. Lett. 116, 071902. http://dx.doi.org/10.1063/1.5140467, URL https://aip.scitation.org/doi/10.1063/1.5140467. publisher: American Institute of Physics.

Zhou, C., Lainé, J., Ichchou, M., Zine, A., 2016. Numerical and experimental investigation on broadband wave propagation features in perforated plates. Mech. Syst. Signal Process. 75, 556–575. http://dx.doi.org/10.1016/j.ymssp.2015.12.006, URL https://www.sciencedirect.com/science/article/pii/S0888327015005555.